Observations of traveling ionospheric disturbances driven by gravity waves from sources in the upper and lower atmosphere

Paul Prikryl[1], David R. Themens[1,2], Jaroslav Chum[3], Shibaji Chakraborty[4], Robert G. Gillies[5], James M. Weygand[6]

[1]Physics Department, University of New Brunswick, Fredericton, NB, Canada
[2]School of Engineering, University of Birmingham, Birmingham, UK
[3]Institute of Atmospheric Physics CAS, Prague, Czech Republic
[4]Center for Space Science and Engineering Research, Virginia Tech, Blacksburg, VA, USA
[5]Department of Physics and Astronomy, University of Calgary, Calgary, AB, Canada
[6]Earth, Planetary, and Space Sciences, University of California, Los Angeles, CA, USA

Correspondence to: Paul Prikryl (paul.prikryl@unb.ca)

Abstract

At high latitudes, the solar wind-magnetosphere-ionosphere-thermosphere coupling modulates the dayside ionospheric convection and currents that generate gravity waves driving equatorward propagating medium- to large-scale traveling ionospheric disturbances (TIDs). At mid latitudes, extratropical cyclones are sources of gravity waves driving medium-scale TIDs. Multi-instrument observations of TIDs, including the Poker Flat Incoherent Scatter Radar (PFISR), the Super Dual Auroral Radar Network (SuperDARN), the multipoint and multifrequency continuous Doppler sounders, and the GNSS total electron content (TEC) mapping technique, are presented. PFISR measured electron density altitude profiles, from which TIDs are obtained by a filtering method to remove background densities. SuperDARN observed dayside pulsed ionospheric flows at high latitudes and ground scatter power modulated by equatorward propagating TIDs that were also observed in the detrended GNSS TEC. At mid latitudes, eastward to southeastward propagating medium-scale TIDs were observed in the detrended TEC maps and by multi-frequency and multi-point continuous HF Doppler sounding system that can determine TID propagation velocities and azimuths. The aim of this study is to attribute the observed TIDs to atmospheric gravity waves generated by auroral sources in the lower thermosphere, or gravity waves generated in the troposphere by mid-latitude weather systems. At high latitudes, the horizontal equivalent ionospheric currents are estimated from the ground-based magnetometer data using an inversion technique. At mid latitudes, the cases of eastward to southeastward propagating TIDs are attributed to gravity waves that are generated by geostrophic adjustment processes and shear instability in the intensifying low-pressure systems and are identified in the stratosphere using the ERA5 meteorological reanalysis.

1. Introduction

The theory governing the propagation and effects of AGWs in the ionosphere was developed by Hines (1960) and their ionospheric sources have been recognized (Chimonas, 1970; Chimonas and Hines, 1970; Testud, 1970; Richmond, 1978). The relationship between atmospheric gravity waves (AGWs) and traveling ionospheric disturbances (TIDs) has been well established (Hocke and Schlegel, 1996). Global propagation of medium- to large-scale GWs/TIDs has been linked to auroral sources (Hunsucker, 1982; Hajkowicz, 1991; Lewis *et al.*, 1996; Balthazor and J., 1997). The Worldwide Atmospheric Gravity-wave Studies (WAGS) program (Crowley and Williams, 1988; Williams *et al.*, 1993) showed that large-scale TIDs originate in auroral latitudes.

TIDs driven by AGWs that originate in the lower atmosphere come from a variety of sources, including tropospheric weather systems (Bertin, Testud and Kersley, 1975; Bertin *et al.*, 1978; Waldock and Jones, 1987; Nishioka *et al.*, 2013; Azeem *et al.*, 2015). Other known causes AGWs/TIDs are solar flares (Zhang et al., 2019), total solar eclipses (Zhang *et al.*, 2017; Mrak *et al.*, 2018), volcanic eruptions, earthquakes, and tsunamis (Yu, Wang and Hickey, 2017; Nishitani *et al.*, 2019; Themens *et al.*, 2022).

Most of the early observations of TIDs were obtained by HF Doppler sounders, HF radars, and incoherent scatter radars (Hunsucker 1982). More recently, the GNSS-derived total electron content (TEC) measurements have become a commonly used technique to observe medium- to large-scale TIDs (e.g., Afraimovich et al., 2000; Cherniak and Zakharenkova, 2018; Cheng et al., 2021; Nykiel et al., 2024). Large-scale TIDs (LSTIDs) have wavelengths greater than 1000 km and propagate at speeds 400-1000 m/s, while medium-scale TIDs (MSTIDs) have wavelengths of several hundred kilometers and tend to propagate at speeds of 250–1000 m/s (Hunsucker, 1982).

van de Kamp et al. (2014) described two techniques to detect TIDs, one using the EISCAT incoherent scatter radar near Tromsø, and the other using the detrended GPS TEC data. They determined parameters characterizing TIDs and studied an event of January 20, 2010. While these authors did not investigate the origin of the TIDs they suggested that the AGWs were most likely generated at low atmospheric layers. Using the EISCAT Svalbard radars on February 13, 2001, Cai et al. (2011) observed moderately large-scale TIDs propagating over the dayside polar cap that

72   were generated by the nightside auroral heating. It is noted that both these TID events occurred on

73   days following arrivals of corotating interaction regions (CIRs) at the leading edge of solar wind

74   high-speed streams that triggered moderate geomagnetic storms.

75

76   Frissell et al. (2016) concluded that polar atmospheric processes, namely the polar vortex, rather

77   than space weather activity are primarily responsible for controlling the occurrence of high-latitude

78   and midlatitude winter daytime medium-scale TIDs (MSTIDs). This paper has been frequently

79   cited to justify suggestions of polar vortex as a source of the observed MSTIDs, particularly when

80   geomagnetic activity is low. Recent papers (Becker et al., 2022; Bossert et al., 2022; Vadas et al.,

81   2023) discussed methods for assessing vortex generated GWs from model output. Vadas et al.

82   (2023) discussed observations of polar vortex generated GWs and subsequent secondary GW

83   generation in the polar region. Becker at al. (2022) performed simulations focusing on multi-step

84   vertical coupling by primary, secondary, and higher-order gravity waves of wintertime

85   thermospheric gravity waves and compared them with observed perturbations of total electron

86   content. They demonstrated that gravity waves generated from lower altitudes can propagate

87   equatorward. Bossert et al. (2022) discussed a strong TID/TAD event observed during a sudden

88   stratospheric warming (SSW) on January 18-19, 2013, and suggested that the large-scale

89   TIDs/TADs were related to geomagnetic activity despite low Kp index. Thus, it is important to

90   continue discussing possible sources of GWs in the lower and upper atmosphere.

91

92   The solar wind coupling to the dayside magnetosphere (Dungey, 1961, 1995) generates variable

93   electric fields that map to the ionosphere driving the $E \times B$ ionospheric convection observed by

94   SuperDARN HF radars and ionospheric currents observed by network of ground-based

95   magnetometers. The mechanisms for energy transfer to the thermosphere can be Joule heating,

96   precipitation, or ion drag by Lorentz force (Richmond, 1979; Nishimura et al., 2020; Deng et al.,

97   2019). Nykiel et al. (2024) found that Joule heating is a primary energy source for the night-time

98   LSTIDs triggered in the auroral region, while the daytime LSTIDs can be also driven by

99   precipitating particles in the polar cusp. On the dayside, pulsed ionospheric flows (PIFs), that are

100   known to be associated with poleward moving auroral forms (precipitation), have been observed

101   to generate AGWs, which in turn modulate ionospheric densities resulting in MSTIDs propagating

102   equatorward observed by SuperDARN radars (Samson *et al.*, 1989; 1990; Prikryl *et al.*, 2005,

103   2022).

104

105 In this study, even in the case when geomagnetic activity is very low, PIFs are found to be the

106 source of AGWs/TIDs observed by PFISR and SuperDARN (Section 3.1). In other cases, the

107 AGWs/TIDs that were generated by solar wind Alfvén waves coupling to the dayside

108 magnetosphere are investigated in Section 3.2. The equatorward propagating TIDs were observed

109 in the detrended vertical vTEC and the radar ground-scatter power focused and defocused by TIDs

110 moving equatorward.

111

112 The tropospheric convection is often a source of gravity waves that propagate into the upper

113 atmosphere driving TIDs (e.g., Azeem, 2021; and references therein). In this study, gravity waves

114 generated in the troposphere by geostrophic adjustment processes and shear instability (Uccellini

115 and Koch, 1987) are considered to drive TIDs propagating eastward to southward that were

116 observed in the detrended vTEC maps and by the HF Doppler sounding system (Section 4). To

117 our knowledge, this physical mechanism has not been considered as a source of TIDs. The ERA5

118 meteorological reanalysis is used to show the gravity waves propagating into the stratosphere,

119

120 The aim of this study is to attribute the observed TIDs to sources in the upper (Section 3), and the

121 lower (Section 4) atmosphere. These observations show that AGWs provide both downward and

122 upward vertical coupling of the ionosphere and neutral atmosphere.

123

124 **2. Data sources and methods**

125 Fig. 1 shows a map of instruments used in this study as described below.

126

127 *2.1. Advanced Modular Incoherent Scatter Radar*

128 Data from the Advanced Modular Incoherent Scatter Radar (AMISR) located in Poker Flats, AK

129 (i.e., the Poker Flats Incoherent Scatter Radar - PFISR) was used in this study. AMISR radars use

130 phased-array beam-forming techniques on a pulse-to-pulse timescale to effectively sample various

131 look directions simultaneously (Heinselman and Nicolls (2008)). These radars have been used to

132 investigate gravity wave propagation (Nicolls and Heinselman, 2007; Vadas and Nicolls, 2008).

133 PFISR is located at the Poker Flat Research Range (65.1°N, 147.5°W) near Fairbanks, Alaska.

134 Due to its phased-array system, PFISR (like other AMISR systems) is able to operate in a variety

135 of different ionospheric sampling modes (often these modes can even be run simultaneously by

136   interleaving different pulse sequences). During the time of interest for this study (January 8-9,

137   2013), PFISR was running a 7-beam mode with interlaced Long Pulse (LP) and Alternating Code

138   (AC) modes. Typically, the LP data is primarily used for sampling the F-region, while the AC

139   mode allows better resolution of E-region densities and parameters. In this study, the LP electron

140   density data from beam 2 of this experiment (elevation 52.5º and azimuth -7.8º) are used. The

141   electron densities measured by an ISR such as PFISR are determined from the total signal power

142   returned from a given range gate. The LP mode in this experiment had a range resolution of 25

143   km, resulting in an altitude resolution of 19.5 km for this beam. To retrieve TIDs, background

144   densities are removed by applying Savitzky-Golay filter (Press and Teukolsky, 1990) that has been

145   used in previous studies (Zhang *et al.*, 2017; 2019). Other types of high-pass filters and detrending

146   methods would produce similar results.

147

148   *2.2. Multi-point and multi-frequency continuous HF Doppler sounding system*

149

150   The multi-point and multi-frequency continuous HF Doppler sounding system operating in the

151   Czech Republic is used to determine propagation velocities and azimuths of TIDs at the specific

152   heights of the signal reflections. The Doppler system consists of three transmitting sites Tx1, Tx2,

153   and Tx3 that are distributed in the western part of the Czech Republic (Tx1: 50.528°N, 14.567°E;

154   Tx2: 49.991°N, 14.538°E; Tx3: 50.648°N, 13.656°E) and receiver Rx located in Prague

155   (50.041°N, 14.477°E). The system is operating at the frequencies of 3.59, 4.65 and 7.04 MHz. The

156   reflection heights depend on the sounding frequency and change during the day and can be

157   obtained from ionograms measured by a nearby digital ionospheric sounder. The frequencies of

158   transmitters operating at a specific frequency are mutually shifted by about 4 Hz at different

159   transmitting sites. Thus, the signals of individual transmitters can be easily distinguished at the

160   receiving site. Locations of the reflection points are assumed in the middle between the individual

161   transmitter–receiver pairs, if projected to the ground. Horizontal distances between the individual

162   reflection points are about 30–50 km. Thus, the system is suitable for propagation analysis of

163   medium-scale TIDs.

164   The processing runs as follows. First, the time evolution of power spectral densities - Doppler

165   shift spectrograms are computed for each signal and the maximum of power spectral density

166   (characteristic Doppler shift) is found with selected time resolution suitable for the TIDs/GWs

167   analysis (30 or 60 s). The obtained time series then serve as an input for the propagation analysis

168   of TIDs (Chum et al., 2021). It should be noted that TID/GW cause movement of plasma and
169   therefore the Doppler shift. The propagation velocities and azimuths are then determined from the
170   time delays between the Doppler shifts recorded for different transmitter-receiver pairs and
171   expected distances of the reflection points in the ionosphere. Three different methods are used to
172   compute time delays between the observed signals (obtained from time series of the Doppler
173   shifts): (a) best beam slowness search, (b) unweighted and (c) weighted least square solution of
174   overdetermined set of equations, based on the time delays obtained for maxima of cross-correlation
175   functions between the individual signals. See Chum and Podolská (2018) for a more detailed
176   description and formulas. Mean values of the propagation velocities calculated from the time
177   delays obtained by these three different methods are presented further. At the same time,
178   uncertainties are estimated from the variance of the obtained results by these three methods as
179   standard deviations. Only velocities that satisfy the following criteria are considered (displayed):
180   the uncertainty of propagation velocity is less than 20% of its absolute value and the uncertainty
181   of azimuth is less than 10°. Analysis for signals Doppler shifts smaller than 0.1 Hz is also not
182   displayed.
183   A 2-D version of propagation analysis (in the horizontal plane) is applied here to analyse longer
184   time intervals (Chum et al. 2021). It should be noted that usable signals (Doppler shifts) are only
185   obtained if the signals reflect from the F2 layer. The Doppler shift of signal reflecting from the E
186   layer is usually negligible. The sounding frequency has also to be smaller than the critical
187   frequency of the ionosphere to receive the reflected signal.
188
189   *2.3. Super Dual Auroral Radar Network (SuperDARN)*SuperDARN constitutes a globally
190   distributed HF Doppler radar network, operational within the frequency range of 8 to 18 MHz,
191   encompassing both the northern and southern hemispheres across various latitudinal bands,
192   including middle, high, and polar zones. Each radar within this network measures the line-of-sight
193   (LoS) component of the drift velocity associated (Chisham et al., 2007; Nishitani et al., 2019). The
194   observations from SuperDARN encompass two principal forms of backscatter, namely, ground
195   and ionospheric scatters. In the case of ground scatter, due to the high daytime vertical gradient
196   in the refractive index, the rays bend toward the ground and are reflected from surface roughness
197   and return to the radar following the same paths. This simulates a one-hop ground-to-ground
198   communication link that passes through the D-region 4 times. Ionospheric scatter is generated
199   when a transmitted signal is scattered from ionospheric irregularities. Typically, ground and

200 ionospheric scatters are associated with relatively lower & higher Doppler velocities and narrower

201 & wider spectral widths, respectively.

202

203 SuperDARN radars are phased-array systems with electronically steerable beams. These radars

204 use a narrow (~3.2°) azimuthal beam and a wide (~25-30°) vertical beam, typically employing an

205 array of 16-20 antennas. A standard 16-20 beam scan provides a field of view approximately 52-

206 62° wide in azimuth, extending from about 180 km to beyond 3000 km in range, with

207 measurements typically taken at 45 km intervals. The radars can operate across a wide range of

208 HF frequencies (8-20 MHz), allowing them to utilize various propagation modes and observe

209 diverse geophysical phenomena. They transmit multi-pulse sequences, and the resulting echoes

210 are processed to calculate multi-lag autocorrelation functions (ACFs). These ACFs, averaged over

211 3-6 seconds, are used to determine power, line-of-sight Doppler velocity, and Doppler spectral

212 width. The resulting fitted ACFs, known as Fitacf data, are generated from raw radar data using

213 version 2.5 of the FITACF algorithm (SuperDARN Data Analysis Working Group et al., 2022).

214

215 In this study, we use line-of-sight (LoS) Doppler velocities and ground scatter observations, i.e.,

216 fitacf2.5 datatsets, to characterize TIDs, with supplementary support from ionospheric convection

217 maps available at the SuperDARN Virginia Tech (VT) website (vt.superdarn.org) to validate their

218 sources. Prior research has demonstrated the utility of both scatter types in studies of pulsed

219 ionospheric flows (PIFs) (McWilliams, Yeoman and Provan, 2000; Prikryl et al., 2002) and TIDs

220 (Samson et al., 1990). MSTID signatures, embedded within radar backscatter, can be used to assess

221 TID phase and propagation direction (Frissell et al., 2014). Previous studies have relied on

222 fitacf2.5-derived parameters, like power and Doppler shift, for such analyses (e.g., Frissell et al.,

223 2014; Inchin et al., 2024). Fig. 1 displays the locations and fields-of-view of radars and other

224 relevant instruments used in this study.

225

226 *2.4. Global Navigation Satellite System (GNSS)*

227 The GNSS data for this were gathered from the same global networks of GNSS receivers used in

228 Themens et al. (2022), which constitute 5200-5800 stations, depending on the period. Examples

229 of the GNSS station distribution in the two local domains can be viewed in Fig. S1 in the

230 Supplement. Using the phase leveling and cycle slip correction method outlined by Themens et al.

231 (2013), whereby phase TEC is leveled to pseudorange TEC using an elevation-weighted mean, the

232   LoS total electron content (TEC) is determined from the differential phase and code measurements

233   of these systems. As detailed in Themens et al. (2015), the satellite biases are acquired from the

234   Center for Orbit Determination in Europe (CODE, ftp://ftp.aiub.unibe.ch/) and receiver biases are

235   determined using a simple Minimization of Standard Deviations approach, wherein a bias is

236   selected by iterating through test biases and minimizing the variance in vertical TEC (vTEC) from

237   all satellites in view over the course of a full day.

238

239   To characterize the TID structures using these data, LoS TEC measurements for each satellite-

240   receiver pair were detrended by first projecting the LoS TEC to vertical TEC (vTEC) using the

241   thin shell approximation at 350-km altitude and subtracting the sliding 60-minute average. More

242   details on this method can be found in Themens et al. (2022). The TEC anomalies are then binned

243   in 0.75-degree latitude and longitude bins for mapping.

244

245   It should be noted, that the detrending used in this analysis largely removes any impact of the

246   satellite biases and receiver biases on the detrended TEC, so the calculation of biases is largely not

247   needed. If we were concerned with timescales closer to the length of a full GNSS arc of lock,

248   residual bias effects on the projected vTEC may need to be considered, but likely would not be

249   significant if at least an approximate bias is used.

250

251   *2.5. Spherical Elementary Current System (SECS)*

252   For this study we will be using the spherical elementary current system (SECS) method to calculate

253   a two-dimensional map of the ionospheric currents. Here we describe the SECS method. A two-

254   dimensional picture of the ionospheric currents can be derived from an array of well-spaced ground

255   magnetometers. The SECS method (Amm and Viljanen, 1999), which has been regularly applied

256   to the International Monitor for Auroral Geomagnetic Effects (IMAGE) ground magnetometer

257   array, can calculate the equivalent ionospheric currents (EICs), which are parallel to Earth's

258   surface, and the SEC amplitudes, which are a proxy for the field-aligned-currents. The SECS

259   technique defines two elementary current systems: a divergence-free elementary current system

260   with currents that flow entirely within the ionosphere and a curl-free current system whose

261   divergences represent the currents normal to the ionosphere. The superposition of these

262   divergence-free and curl-free current systems can reproduce a vector field on a sphere. For this

263   study we only calculate the divergence-free (equivalent ionospheric) currents, which are a

264   combination of the real Hall and Pedersen currents. The temporal and spatial resolutions of the
265   equivalent ionospheric currents are 10 s and 6.9° geographic longitude by 2.9° geographic latitude
266   (see, Amm et al., 2002 for more details). In general, the EICs are calculated from a matrix inversion
267   of ground magnetic disturbances. One of the important features of this technique is that it requires
268   no integration time of the magnetometer data. Unlike like AMPERE currents, which requires a 10
269   min integration time for many of the spacecraft to cross the polar region or the SWARM currents
270   that only provide a slice of the ionospheric currents as they cross the auroral region. The technique
271   (see, Weygand et al. 2011; their Figure 1) has been applied to magnetometers located in North
272   America and Greenland for the last 15+ years (Weygand et al. 2012; 2016).

273

274   In the European sector, ground magnetic perturbances due to the ionospheric currents and 1D
275   equivalent currents estimates are provided by the International Monitor for Auroral Geomagnetic
276   Effects (IMAGE) array of magnetometers.

277

278   *2.6. S*olar wind data
279   The solar wind data are provided by the OMNIWeb (http://omniweb.gsfc.nasa.gov) (King and
280   Papitashvili, 2005) and the Goddard Space Flight Center Space Physics Data Facility
281   (https://spdf.gsfc.nasa.gov/index.html). The magnetic field, proton density and velociy
282   measurements obtained by Advanced Composition Explorer (ACE) (Smith *et al.*, 1998) are used.

283

284   *2.7. ERA5 meteorological reanalysis*
285   The hourly reanalysis dataset ERA5 with spatial resolution of 0.25 x 0.25 degree (Hersbach et al.,
286   2020) is a product of the European Centre for Medium-Range Weather Forecasts (ECMWF). The
287   300-hPa geopotential height, horizontal winds at 300 hPa, and the divergence of the horizontal
288   wind at 150-hPa level are used. The alternating bands of convergence and divergence have been
289   interpreted by Plougonven and Teitelbaum (2003) as gravity waves propagating to the lower
290   stratosphere.

291

292   **3. AGWs/TIDs originating from lower thermosphere at high latitudes**

293

294   Solar wind high-speed streams (HSSs) are associated with high-intensity, long-duration
295   continuous auroral electrojet activity (HILDCAAs) that includes auroral substorms (Tsurutani and

296 Gonzalez, 1987; Tsurutani et al., 1990, 1995). HILDCAAs are caused by trains of solar wind
297 Alfvén waves (Belcher and Davis, 1971) that couple to the magnetosphere-ionosphere system
298 (Dungey, 1961, 1995). This coupling extends to the neutral atmosphere and ionosphere because it
299 is a source of aurorally excited gravity waves. Solar wind modulation of cusp particle signatures
300 was associated with ionospheric flows (Rae et al., 2004). Solar wind Alfvén waves can modulate
301 ionospheric convection and currents, most directly on the dayside, producing polar cap density
302 patches and AGW/TIDs (Prikryl *et al*., 1999, 2005, 2022).

303

304 We now investigate cases of TIDs observed at high latitudes using the PFISR, SuperDARN and
305 GNSS data supported by solar wind and ground-based magnetometers. In Section 3.1, we examine
306 one case when PFISR in Poker Flat, Alaska, observed TIDs during geomagnetically quiet period
307 on January 8, 2013 in the context of solar wind coupling to show evidence that the observed TIDs
308 originated in the high-latitude dayside ionosphere poleward of Alaska, where there are no ground-
309 based magnetometers to sense the ionospheric currents, but ionospheric convection is observed by
310 SuperDARN. In Section 3.2, we present more examples of TIDs generated by solar wind-M-I-T
311 coupling on the dayside. The TIDs were observed in the North America and Europe by
312 SuperDARN and in the detrended vTEC.

313

314 *3.1. Event of January 8/9, 2013*
315 In the period from January 8 to 15 the PFISR beams scanned electron densities, N_e (cm^{-3}), at
316 altitudes from 150 to 500 km. In the detrended TEC maps over Alaska (https://aer-nc-
317 web.nict.go.jp/GPS/GLOBAL/MAP/2013/008/index.html) the equatorward propagating TIDs
318 were observed on each day during the daytime hours when the PFISR density data show signatures
319 of downward propagating phase of TIDs. Fig. 2a shows N_e in logarithmic scale as a function of
320 altitude observed by the radar beam 2 at temporal resolution of 3 min between 18:00 and 03:00
321 UT (09:00 and 18:00 LT) on January 8-9, 2013. The downward propagating phase of TIDs is
322 readily seen superposed on the background of high daytime densities. To remove the background
323 and highlight the TIDs with periods > 40 min the time series for each altitude are detrended using
324 a 33-point wide Savitzky-Golay filter (4th degree, 2nd order) (Fig. 2b). To show the equatorward
325 propagation of the TIDs across Alaska, Fig. 2c shows the detrended GNSS vTEC mapped at
326 latitude bins along the longitude of the PFISR.

327

328   The geomagnetic activity on January 8 was low, with the *Kp*-index ≤ 1 except for a peak of 3- in

329   the last 3-hourly interval caused by a substorm that occurred in the European sector. The

330   northernmost magnetometer in Alaska in Barrow observed the north-south *X*-component magnetic

331   field perturbation of ~230 nT at 17:10 UT (see Fig. S2 in the Supplement) indicating the westward

332   electrojet. At this time, the IMF was pointing dawnward ($B_y < 0$) and eastward flows (see Fig. S3a

333   in the Supplement) in the dawn convection cell corresponded with the westward electrojet sensed

334   in Barrow. After 18:00 UT, as the IMF B_y reversed to duskward (Figure 2c), the convection cells

335   receded further poleward of Alaska and the convection pattern become dominated by the dusk cell

336   (see Fig. S3b in the Supplement). At this time, the distant westward electrojet over Beaufort Sea

337   could no longer be detected by magnetometers.

338

339   The King Salmon Radar (KSR) beam 9 pointing northwest over the East Siberian Sea observed

340   positive (towards the radar) line-of-sight (LoS) velocities indicating quasiperiodic (20-50 min)

341   pulsed ionospheric flows (PIFs; Fig. 3a) in the dawn convection cell. At near ranges, the KSR

342   radar observed enhancements in the sea scatter power (Fig. 3b) caused by a series of equatorward

343   propagating TIDs. The Prince George Radar (PGR) beam 1 also observed the TIDs in the ground

344   scatter power with periods similar to those of PIFs and the TIDs observed by PFISR (Fig. 2). To

345   show the actual TID location in the ionosphere, instead of the slant range the ground-scatter range

346   mapping (Bristow, Greenwald and Samson, 1994; Frissell *et al.*, 2014) is applied in Fig. 3d.

347   Projected to the direction of beam 1, the estimated TIDs wavelengths ranged between ~200 and

348   500 km, and phase velocities between ~100 and 300 m/s.

349

350   The IMF southward turnings are expected to modulate the reconnection rate at the magnetopause

351   leading to intensifications of the ionospheric convection/currents in the cusp footprint. One of the

352   convection enhancements can be viewed in Fig. S3b in the Supplement. Pulsed ionospheric flows

353   are known to be associated with particle precipitation in poleward moving auroral forms (Rae et

354   al., 2004). In the cusp, particle precipitation and Joule heating can be comparable energy source

355   for AGWs/TIDs (Nykiel et al., 2024). The time series of the ACE IMF B_y and B_z, as well as the

356   clock angle (B_z, B_y) counted from the geomagnetic north, with the 180° (dotted line) indicating

357   southward turnings of the IMF are shown time-shifted in Fig. 3c. Normalized FFT spectra of the

358   detrended IMF B_z, B_y, and the Prince George radar ground scatter power (beam 1, gate 30, mapped

359   GS range 730 km) are shown in the inset in Figure 3d. The spectra of the IMF B_z and the Prince

360 George radar ground scatter power are very similar thus providing evidence that the generation of
361 TIDs was driven by solar wind coupling to the dayside magnetosphere. The clock angle controls
362 the reconnection rate at the magnetopause (Milan et al., 2012). The TIDs can be approximately
363 associated with southward IMF turnings (positive deflections of the clock angle values towards
364 180° marked by arrows in Fig. 3). Of course, this is an approximate correspondence. The IMF
365 observed by ACE does not represent exactly the IMF impacting the dayside magnetopause. It
366 would require at least a spacecraft in front of the bow shock to monitor the IMF (e.g., Prikryl et al.
367 2002). But the observations of pulsed ionospheric flows (PIFs) and corresponding TIDs points to
368 sources of these TIDs in the high-latitude ionosphere poleward of Alaska. Prikryl et al. (2005; their
369 Figure 2) showed that the observed TID propagation times, horizontal wavelengths and phase
370 velocities deduced from the ground-scatter are consistent with the results of ray tracing of the
371 gravity wave energy from an ionospheric source.

372

373 While we focused here on January 8/9, on each day during the PFISR experiment from January 8
374 to 15 the solar wind-MIT coupling that modulated PIFs in the ionospheric cusp footprint poleward
375 of Alaska launched TIDs that were observed by PFISR, as well as in the GNSS vTEC maps.
376 Similarly, in the European sector, dayside TIDs propagating equatorward from their sources in the
377 cusp over Svalbard were also observed. This can be viewed in Fig. S4 in the Supplement, and it is
378 consistent with previous studies of PIFs in the ionospheric cusp resulting in TIDs (Prikryl et al.,
379 2005; 2022).

380

381 *3.2. Events of November 1 and 4-5, 2014*

382

383 Fig. 4 shows the solar wind data indicating arrivals of HSS/CIRs marked by asterisks. The second
384 one triggered a minor geomagnetic storm with the *Dst* index (Gonzalez *et al.*, 1994) reaching
385 maximum negative value of −44 nT on November 4. Solar wind Alfvén waves permeate HSSs,
386 and along with CIRs, are highly geoeffective when IMF $B_z < 0$ (Tsurutani et al., 1987, 1995, 2006).
387 On November 1 and 5, 2014, the solar wind Alfvén waves are characterized by the Walén relation
388 between velocity *V* and magnetic field *B* (Yang, Chao and Lee, 2020). The components of the
389 corresponding components of the magnetic field (B_y and B_z) and velocity (V_y and V_z) observed by
390 ACE are correlated (Fig. 5a), which is a signature of solar wind Alfvén waves. For November 5,
391 this can be viewed in Fig. S5a in the Supplement.

392

393 In the European sector, the SuperDARN Hankasalmi radar observed PIFs in the cusp over
394 Svalbard, and equatorward propagating TIDs, which were also observed in the detrended vTEC.
395 Figs. 6 and 7 show the ionospheric LoS velocities and the radar scatter power (ground scatter
396 shown in grey color in the velocity plot) observed by the radar beam 11 on November 1 and 5,
397 respectively. The radar ground scatter (Figs. 6b and 7b) at ranges between 1000 and 1800 km
398 shows tilted bands due to equatorward propagating TIDs. Applying the ground scatter mapping
399 method (as already discussed in Section 3.1), the estimated MSTID wavelengths ranged between
400 ~100 and 500 km, and phase velocities between ~100 and 300 m/s (Figs. S6a and S6b in the
401 Supplement).

402

403 The ground magnetic field perturbations of the X-component observed in Ny Ålesund (NAL;
404 https://space.fmi.fi/image/www/index.php) and 1D equivalent currents estimates that use all
405 IMAGE magnetometers are superposed. The radar observed a series of intensifications of the
406 negative (away from the radar) LoS velocities (PIFs) at ranges greater than ~2000 km on the
407 dayside, starting at ~07:00 UT with the onset of ionospheric currents fluctuations sensed by the
408 NAL magnetometer. The solar wind Alfvén waves modulated the dayside ionospheric currents
409 launching AGWs driving the equatorward propagating TIDs observed in the radar ground scatter
410 at ranges below ~2000 km. For November 1, Figs. 5b and 5c show the FFT spectra of detrended
411 time series of IMF B_z, solar velocity V_z, the NAL X-component, and the Hankasalmi radar ground
412 scatter power (beam 11, gate 25, slant range 1305 km) displaying peaks at similar
413 frequencies/periods. For November 5, the FFT spectra can be viewed in Figs. S5b and S5c in the
414 Supplement.

415

416 Figs. 8a and 8b show the TIDs observed in the detrended vTEC as alternating positive and negative
417 anomalies mapped along longitude of 15°E on November 1 and 5, respectively. The equatorward
418 propagating TIDs were observed at mid latitudes, but it is difficult to estimate their propagation
419 speeds as they appear to have been disrupted due to interference with TIDs from tropospheric
420 sources moving eastward to southeastward that are discussed in Section 4.

421

422 The arrival of the HSS/CIR on November 4 triggered a minor geomagnetic storm. Similar to cases
423 reported previously (Prikryl et al., 2022), intense ionospheric currents in the North American

424   sector auroral zone launched TIDs that were observed by the midlatitude SuperDARN radars and

425   the detrended TEC. Before 4:00 UT at radar frequency at 11.5 MHz, the Fort Hays West (FHW)

426   midlatitude radar beam 12 looking northwest over the central Canada observed the ionospheric

427   scatter showing enhancements in the positive LoS velocities (toward the radar; Fig. 9a) due to

428   fluctuating eastward ionospheric flows at the equatorward edge of an expanded dawn convection

429   cell associated with the fluctuating westward electrojet. The ionospheric currents were sensed by

430   magnetometers, including one in Fort Simpson (FSIM; www.carisma.ca/). The X component of

431   the ground magnetic field and time series of the latitudinal maxima in EICs at the longitude of

432   120°W, are superposed. After 14:00 UT, when the radar frequency was set to 15 MHz, the HF

433   propagation allowed to observe TIDs in the ground scatter. The ground scatter slant ranges

434   between 1000 and 3000 km correspond to the mapped ground scatter ranges between 200 and 1200

435   km.

436

437   Two major intensifications of the westward electrojet at ~13:10 and 14:10 UT (Fig. 9b) launched

438   LSTIDs observed in the ground scatter starting at ~14:00 and 15:00 UT. The mapped EICs in Fig.

439   10a show the first major intensification of the westward electrojet (the EIC maxima at each

440   longitude are highlighted) that was followed by the second intensification an hour later (Fig. 9b).

441   They launched equatorward propagating LSTIDs (wavelength greater than 1000 km) observed in

442   the detrended vTEC maps (Fig. 10b). Fig. 11a shows the LSTIDs between 13:00 and 16:00 UT in

443   the detrended vTEC mapped along longitude of 100°W in the North American sector. The

444   approximate equatorward propagation speeds were between 500 and 800 m/s.

445

446   In the European sector, during the most disturbed time following the HSS/CIR arrival on

447   November 4 the dayside auroral oval expanded down to latitude ~63°N. Fig. 11b shows the

448   equivalent ionospheric currents estimated from the IMAGE magnetometers. LSTIDs (Fig. 10c)

449   that were launched by intensifications of the east electrojet were observed propagating

450   equatorward at speeds between 400 and 500 m/s in mid latitudes are mapped along longitude of

451   15°W between 11:00 and 18:00 UT (Fig. 11b).

452

453   In summary, the cases discussed in Sections 3.1 and 3.2 highlight the importance of solar wind

454   coupling to the M-I-T system, particularly on the dayside, in the generation of AGWs/TIDs. The

455 fluctuations of the IMF, sometimes Alfvénic, modulate PIFs and ionospheric currents in the cusp

456 launching GW/TIDs.

457

458 **4. AGWs/TIDs originating from sources in the troposphere**

459

460 MSTIDs caused by GWs with periods of 10-40 min propagating obliquely upward in the

461 thermosphere/ionosphere have been studied using multi-frequency and multi-point continuous HF

462 Doppler sounding system located in the western part of Czechia (Chum et al., 2021). The 2-D

463 propagation analysis of the HF Doppler sounders data is applied to available signals to exclude

464 data gaps and to select time intervals in which the phase shifts/time delays between signals

465 corresponding to different sounding paths (transmitter-receiver pairs) were approximately

466 constant.

467

468 The observed azimuths depend on season with southeastward propagation more likely in winter

469 months, suggesting that cold season low pressure systems in the northeast Atlantic are sources of

470 the GWs, which supports previously published results (Azeem et al., 2018) and points to winter

471 jet stream as a likely source of GWs. In this section we examine such cases and trace TIDs in the

472 detrended GNSS TEC maps (Fig. 12) and observed by the HF Doppler sounders propagating

473 eastward to southeastward from intensifying low-pressure weather systems over the east Atlantic.

474 The animated TEC maps can be viewed in the Supplement Video, which also shows the

475 equatorward propagating TIDs that originated at high latitudes as discussed in Section 3.

476

477 *4.1. Events of November 1-8, 2014*

478 Spectral and propagation analysis for all available 7.04 MHz signals from November 1 to 8, 2014

479 was performed (Fig. 13). Only daytime values are available because the critical frequency foF2 is

480 too low at night (most of the nights are also not available at 4.65 MHz). On November 6 an

481 enhanced noise (electromagnetic interference) prevented reliable analysis for a substantial part of

482 the day. Fig. 13b shows dynamic spectra (periodograms) of Doppler shift signal obtained as the

483 average of the maxima of three power spectral densities corresponding to three different

484 transmitter – receiver pairs (Section 2) shown in Fig. 13a (including artificial offsets). The

485 observed periods (Fig. 13b) range from 10 to about 40 min. The propagation azimuths (Fig. 13c)

486 were mostly from 100 to about 160° (waves propagating south-eastward). In all cases, the azimuth

487   is only plotted if the averaged Doppler fluctuations exceeded 0.12 Hz, the estimate of uncertainty

488   of azimuth is less than 10° and the estimate of uncertainty in velocity is less than 10%. The phase

489   velocities fluctuated typically between 100 and 200 m/s. Fig. 14 shows the analysis results on an

490   expanded time scale to better see the TID characteristics for November 8.

491

492   During the period from November 1 to 8, 2014, the south-eastward propagating MSTIDs were

493   observed by the HF sounders and detrended vTEC. Low-pressure systems deepening over the

494   North-east   Atlantic,   shown   in   the   surface   pressure   analysis   charts

495   (https://www.wetter3.de/archiv_ukmet_dt.html), were likely sources of these MSTIDs

496   propagating eastward to southeastward, as observed in the detrended vTEC maps (indicated by

497   arrows in Figs. 12a,b) on November 1 and 8, 2014. At the same time, the vTEC maps on both days

498   also reveal equatorward propagating TIDs at latitudes down to ~50°N that originated in the cusp

499   ionospheric footprint over Svalbard, as already discussed in Section 3.2.

500

501   The Doppler shift frequencies (Fig. 14a) recorded at frequency 7.04 MHz on November 1 and 8,

502   2014 show temporal evolution of power spectral densities (color-coded arbitrary units) of received

503   signals that correspond to three different transmitter-receiver pairs. There was enhanced noise due

504   to the electromagnetic interference on 8 November from about 9:30 to 12:30 UT. The straight

505   horizontal line in the upper signal trace in the spectrogram corresponds to ground wave from one

506   of the transmitters, located only ~7 km from the receiver. The middle and bottom signal traces in

507   the spectrogram correspond to other two transmitters. As described in more detail in Section 2.2,

508   the use of well correlated signals at two or three different frequencies makes it possible to

509   determine a 3-D phase velocity vector. The results that are summarized in Table S1 in the

510   Supplement separately for the observation at frequencies of 4.65 and 7.04 MHz show mostly

511   similar values of horizontal velocities (ranging from ~100 to 200 m/s) and azimuths (ranging from

512   ~90 to 145°).

513

514   *4.2. Events of December 5-7, 2024*

515   Similarly to events discussed in Section 4.1, low-pressure systems deepening over the North-east

516   Atlantic on December 5-7 were likely sources of GWs driving the observed southeastward

517   propagating MSTIDs (Fig. 12c). To further support the results in Section 4.1 we analyzed these

518   recent events recorded at 4.65 and 7.04 MHz. Due to the critical frequency of the ionosphere 4.65

519 MHz allows to obtain longer time intervals with usable signals but with smaller amplitudes. The
520 signals at 7.04 MHz reflect from higher altitudes where the amplitudes are larger. The results of
521 the spectral and propagation analysis for all available 7.03 MHz signals for December 5-7, 2024
522 are shown in Fig. 15. Fig. 15b shows dynamic spectra of Doppler shift signal obtained as the
523 average of the frequencies corresponding to the maxima of the three power spectral densities for
524 the three different transmitter – receiver pairs shown in Fig. 15a (including artificial offsets, which
525 were removed before the spectral and propagation analysis). The observed periods of TIDs/GWs
526 (Fig. 15b) range from a few minutes up to an hour. The propagation azimuths (Fig. 15c) were
527 mostly around 140 deg. (southeastward) and phase velocities fluctuated typically between 150 and
528 290 m/s.

529

530 *4.3. Comparison between TIDs observed in the detrended vTEC maps and by the HF Doppler*
531 *sounding system*
532 The Doppler shift spectrograms recorded at frequency 7.04 MHz on November 8, 2014 and
533 December 5, 2024 are shown in Fig. 16a (top panels). In Fig. 16b (middle panels), the detrended
534 vTEC mapped along the latitude of 50° shows eastward propagating TIDs towards the longitude
535 of the HF sounding system with estimated approximate velocities shown. The bottom panels (Fig.
536 16c) show time series of the detrended vTEC at longitude of 7°E with the normalized FFT spectra
537 shown in the insets.

538

539 In November 2014, the amplitudes of MSTIDs observed in the detrended vTEC and by the HF
540 Doppler sounder were relatively small, and the coverage by GNSS receivers at longitudes greater
541 than 10°E was sparse. In contrast, in December 2024, the GNSS coverage significantly improved,
542 and the amplitudes of MSTIDs observed both in the vTEC and by HF Doppler sounder were much
543 larger.

544

545 While it is difficult to compare in detail the results obtained by these two very different techniques
546 (one based on the global mapping of vTEC using the thin shell approximation at 350-km altitude,
547 and the other local measurements dependent on the HF propagation and the critical frequency for
548 reflection altitude), the phase velocities (Fig. 16b) and periods (Fig. 16c) of TIDs estimated from
549 the detrended vTEC are similar to those obtained by the HF Doppler sounder as discussed in
550 Sections 4.1 and 4.2 (Figs, 14 and 15).

551

552 More cases of eastward to south-eastward propagating MSTIDs observed by the HF Doppler

553 sounder and in the detrended vTEC observed in 2014 on November 1, 3 and 7 (see Fig. S7-S9 in

554 the Supplement), November 22 and 24, December 9-10, and December 24, were also associated

555 with intense low-pressure systems in the North-east Atlantic.

556

557 *4.4. Physical mechanism of GW generation in the troposphere*

558 While tropospheric convection is a common source of gravity waves (e.g., Azeem, 2021), no deep

559 convection could be identified in the cold fronts of low-pressure systems over the North-east

560 Atlantic (GIBBS). Mesoscale gravity waves generated by geostrophic adjustment processes and

561 shear instability have been observed (Uccellini and Koch, 1987; Koch and Dorian, 1988).

562 Plougonven and Zhang (2014) reviewed the current knowledge and understanding of gravity

563 waves near jets and fronts. Plougonven and Teitelbaum (2003; their Figure 2) showed patterns of

564 alternating bands of convergence and divergence in maps of divergence of the horizontal wind for

565 the lower stratosphere, which have been interpreted as the signature of inertia-gravity waves

566 propagating upwards above the tropopause. A conceptual model of a common synoptic pattern has

567 been identified with a source of gravity waves near the axis of inflection in the 300-hPa

568 geopotential height field (Koch and O'Handley, 1997; their Figure 2).

569

570 In Sections 4.1 and 4.2, the cases of MSTIDs on November 1 and 8, 2014 and December 5, 2024

571 propagating eastward to southeastward observed in the detrended vTEC maps (Fig. 12) and by the

572 HF Doppler sounding system (Figs. 13, 14 and 15) are attributed to sources in the troposphere,

573 namely deepening low pressure weather systems. This is consistent with the conceptual model

574 referenced above. Using the ERA5 reanalysis (Hersbach *et al.*, 2020), Fig. 17 shows the 300-hPa

575 geopotential height, approximate axis of inflection (a probable source region of gravity waves that

576 is indicated by red dashed line), and horizontal winds at 300 hPa for the three events in 2014 and

577 2024. Fig. 17b shows the divergence of the horizontal wind at 150-hPa level. The alternating bands

578 of convergence and divergence are similar to those interpreted by Plougonven and Teitelbaum

579 (2003) as gravity waves propagating to the lower stratosphere. Other cases of MSTIDs on

580 November 3 and 7 can be viewed in Figs. S7 and S8 in the Supplement. Mesoscale GWs

581 propagating eastward and upward into the stratosphere generated by geostrophic adjustment

582 processes and shear instability may be common and could be driving MSTIDs.

583

5. Discussion

The solar wind – MIT coupling is known to modulate the intensity of ionospheric currents, including the auroral electrojets, which in turn launch atmospheric gravity waves causing TIDs. The cases of dayside equatorward propagating TIDs were observed with PFISR, SuperDARN, and detected in the detrended GNSS vTEC maps. This is consistent with previously published results and interpretations (e.g., Prikryl et al. 2022; and references therein). The dayside TIDs are commonly generated in the ionospheric footprint of the cusp. They were observed every day over Alaska during the PFISR experiment (8-15 January 2013) and in Europe (1-8 November 2014).

In Section 3.1, we have shown evidence that even during a geomagnetically very quiet period the TIDs that were observed by PFISR in Alaska can be attributed to sources at high latitudes (Fig. 3). Quasiperiodic intensifications of the high-latitude ionospheric convection that were the source of these TIDs were observed poleward of Alaska over the East Siberian and Beaufort Seas. The ionospheric currents associated with PIFs could not be detected by ground magnetometers, and the *Kp* index indicated a quiet period. The ionospheric footprint of the cusp where the pulsed ionospheric flows and associated currents are sources of TIDs may be located further poleward of any ground magnetometers. Low geomagnetic activity is often taken as a pretext to dismiss auroral sources of TIDs. Throughout the PFISR experiment from January 8 to 15, 2013 the TIDs that were observed on the dayside resulted from the solar wind-MIT coupling that modulated PIFs in the ionospheric cusp footprint poleward of Alaska. Similarly, in the European sector.

The importance of solar wind coupling to the M-I-T system, particularly on the dayside, for the generation of AGWs/TIDs (Prikryl et al. 2005) is further highlighted in Section 3.2 by cases where solar wind Alfvén waves modulated PIFs and ionospheric currents in the cusp launching AGWs/TIDs.

Regarding TIDs originating from the troposphere, there has been plentiful evidence of neutral atmosphere-ionosphere coupling via atmospheric gravity waves propagating into the upper atmosphere from sources in the lower atmosphere including convective storms (Alexander, 1996). Azeem and Barlage (2018) and Vadas and Azeem (2021) presented cases of convective storm generating TIDs, which exhibited partial to full concentric, or almost plane-parallel phase fronts. The latter TIDs were generated by extended squall line (Azeem and Barlage, 2018). However, in the cases discussed in Section 4.1 there was no significant convection in the cold fronts that would

615   generate such TIDs. The eastward propagating MSTIDs observed in the detrended vTEC maps
616   and by the HF originated from low pressure sounding system were likely driven by GWs generated
617   by geostrophic adjustment processes and shear instability in the troposphere. Geostrophic
618   adjustment processes (Uccellini and Koch, 1987) generating gravity waves have not been
619   previously considered as sources of TIDs. This is supported by the ERA5 meteorological
620   reanalysis showing the GWs in the lower stratosphere.

621

622   The occurrence of eastward propagating MSTIDs at mid latitudes over Europe is very common in
623   the cold season, and their association with low-pressure systems can be readily seen browsing the
624   archive of detrended TEC maps (https://aer-nc-web.nict.go.jp/GPS/EUROPE/MAP/#2014). An
625   assortment of such cases for December 2014 can be viewed in the Supplement Figures S10-S14.
626   At the same time, the animations of TEC maps provided in the archive show equatorward
627   propagating TIDs, including LSTIDs, originating at high latitudes that are generated by solar wind-
628   M-I-T coupling. Dayside equatorward propagating TIDs that were observed in the detrended vTEC
629   in Europe (15°E), the U.S. (100°W) and Alaska (148°W) on December 5, 2024 can be viewed in
630   the Supplement Figure S15.

631

632   In this study, a multi-instrument approach is used to trace/attribute the observed TIDs to sources
633   of AGWs in the upper and lower atmosphere, and to identify physical mechanisms. The solar wind
634   coupling to the M-I-T system generates equatorward propagating TIDs on the dayside even during
635   geomagnetically quiet conditions. This is important, because the auroral sources of TIDs observed
636   during quiet conditions are often not considered or dismissed. On the other hand, intensifying low
637   pressure weather systems generate AGWs propagating to the lower stratosphere and beyond,
638   driving TIDs even when there is no significant tropospheric convection. More work needs to be
639   done to better understand such cases, and many aspects of the system as a whole should be
640   considered when determining the source of TIDs, as simple metrics/indices hide critical details.

641

642   **6. Summary and conclusions**
643   Traveling ionospheric disturbances are observed by radars, Doppler sounders, and the GNSS TEC
644   mapping technique. Medium- to large-scale TIDs propagating equatorward were generated by
645   solar wind coupling to the dayside magnetosphere-ionosphere-thermosphere modulating
646   ionospheric convection and currents, including auroral electrojets. MSTIDs that were observed

over Alaska by the Poker Flat incoherent scatter radar and by two SuperDARN radars are attributed to gravity waves generated in the ionospheric cusp footprint poleward of Alaska even when geomagnetic activity was low. Dayside MSTIDs were observed every day over Alaska during the 7-day PFISR experiment. In another case, following the arrival of high-speed solar wind stream that triggered a minor geomagnetic storm, major intensifications of the westward electrojet over the North American sector launched LSTIDs observed by a mid-latitude SuperDARN radar and in the detrended global TEC maps. In the European sector, the equatorward propagating TIDs are attributed to solar wind Alfvén waves coupling to the dayside magnetosphere modulating ionospheric convection and currents in the cusp footprint over Svalbard. On the other hand, the cases of eastward to southeastward propagating MSTIDs observed at mid latitudes in the detrended GNSS TEC maps and by the HF Doppler sounders in Czechia originated from low pressure weather systems intensifying in the north-east Atlantic. Gravity waves propagating from the troposphere and lower stratosphere were likely generated by geostrophic adjustment processes, which have not been linked to TIDs previously.

Data availability. The solar wind data are provided by the NSSDC OMNI (http://omniweb.gsfc.nasa.gov; NASA, 2022). The ground-based magnetometer data are archived at the website of the Canadian Array for Realtime Investigations of Magnetic Activity (CARISMA) (https://www.carisma.ca/; University of Alberta, 2022), and the IMAGE website at https://space.fmi.fi/image/www/index.php?. The PFISR data are available at https://data.amisr.com/database/61/cal/2014/11/. SuperDARN data are available at https://www.frdr-dfdr.ca/repo/collection/superdarn (FRDR, 2022). Line-of-Sight TEC data can be acquired from the Madrigal database (http://cedar.openmadrigal.org/; CEDAR, 2022) and CHAIN GNSS data are available at http://chain.physics.unb.ca/chain/pages/data_download (CHAIN, 2022).

Equivalent Ionospheric Currents (EICs) derived by the Spherical Elementary Currents Systems (SECS) technique are archived at http://vmo.igpp.ucla.edu/data1/SECS/ (SECS, 2022) and https://cdaweb.gsfc.nasa.gov/pub/data/aaa_special-purpose-datasets/spherical-elementary-and-equivalent-ionospheric-currents-weygand/; https://doi.org/10.21978/P8D62B, Weygand, 2009a; https://doi.org/10.21978/P8PP8X, Weygand, 2009b). The Czech HF Doppler shift spectrograms can be found in the archive at http://datacenter.ufa.cas.cz/.

678 GNSS data for this study were provided by the following organizations: International GNSS

679 Service (IGS), UNAVCO (https://www.unavco.org/data/gps-gnss/gps-gnss.html), Dutch

680 Permanent GNSS Array (http://gnss1.tudelft.nl/dpga/rinex), Can-Net (https://www.can-net.ca/),

681 Scripps Orbit and Permanent Array Center (Garner, http://garner.ucsd.edu/pub/), French Institut

682 Geographique National, Geodetic Data Archiving Facility (GeoDAF,

683 http://geodaf.mt.asi.it/index.html), Crustal Dynamics Data Information System (CDDIS,

684 https://cddis.nasa.gov/archive/gnss/data/daily/), National Geodetic Survey

685 (https://geodesy.noaa.gov/corsdata/), Instituto Brasileiro de Geografia e Estatistica

686 (http://geoftp.ibge.gov.br/informacoes_sobre_posicionamento_geodesico/rbmc/dados/), Instituto

687 Tecnologico Agrario de Castilla y Leon (ITACyL, ftp://ftp.itacyl.es/RINEX/), TrigNet South

688 Africa (ftp://ftp.trignet.co.za), The Western Canada Deformation Array (WCDA,

689 ftp://wcda.pgc.nrcan.gc.ca/pub/gpsdata/rinex), Canadian High Arctic Ionospheric Network

690 (CHAIN, http://chain.physics.unb.ca/chain/pages/data_download), Pacific Northwest Geodetic

691 Array (PANGA, http://www.geodesy.cwu.edu/pub/data/), Centro di Ricerche Sismologiche,

692 Système d'Observation du Niveau des Eaux Littorales (SONEL, ftp://ftp.sonel.org/gps/data),

693 INGV - Rete Integrata Nazionale GPS (RING, http://ring.gm.ingv.it/),RENAG : REseau

694 NAtional GPS permanent (http://rgp.ign.fr/DONNEES/diffusion/), Australian Space Weather

695 Services (https://downloads.sws.bom.gov.au/wdc/gnss/data/),GeoNet New Zealand

696 (https://www.geonet.org.nz/data/types/geodetic), National Land Survey Finland (NLS,

697 https://www.maanmittauslaitos.fi/en/maps-and-spatial-data/positioning-services/rinex-palvelu),

698 SWEPOS Sweden (https://swepos.lantmateriet.se/), Norwegian Mapping Authority (Kartverket,

699 https://ftp.statkart.no/), Geoscience Australia (http://www.ga.gov.au/scientific-

700 topics/positioning-navigation/geodesy/gnss-networks/data-and-site-logs), Institute of

701 Geodynamics, National Observatory of Athens (https://www.gein.noa.gr/services/GPSData/),and

702 European Permanent GNSS Network (EUREF,

703 https://www.epncb.oma.be/_networkdata/data_access/dailyandhourly/datacentres.php).

704 *Author contributions*. PP and RGG contributed to conception and design of the study. PP, DRT,

705 JC, SC, RGG, and JMW acquired the resources and contributed to methodology, software, specific

706 data analysis, visualization, and organized the databases. PP wrote the first draft of the manuscript.

707 All authors contributed to manuscript revision and approved the submitted version.

708 *Competing interests*. The authors declare that they have no conflict of interest.

709 *Acknowledgments.* Infrastructure funding for CHAIN was provided by the Canada Foundation for
710 Innovation and the New Brunswick Innovation Foundation. CHAIN operation is conducted in
711 collaboration with the Canadian Space Agency (CSA). We are grateful to the Australian Bureau
712 of Meteorology, Space Weather Services for the provision of GNSS data. CDDIS is one of the
713 Earth Observing System Data and Information System (EOSDIS) Distributed Active Archive
714 Centers (DAACs), part of the NASA Earth Science Data and Information System (ESDIS) project.
715 Datasets and related data products and services are provided by CDDIS, managed by the NASA
716 ESDIS project. This material is based on services provided by the GAGE Facility, operated by
717 UNAVCO, Inc., with support from the National Science Foundation and the National Aeronautics
718 and Space Administration under NSF Cooperative Agreement EAR-1724794. A. Contributions by
719 the ACE (Norman F. Nees at Bartol Research Institute, David J. McComas at SWRI), NASA's
720 SPDF/CDAWeb, and the NSSDC OMNIWeb are acknowledged. The PFISR was developed under
721 NSF cooperative agreement ATM-0121483, and the data collection and analysis were supported
722 under NSF cooperative agreement ATM-0608577. The authors acknowledge the use of
723 SuperDARN data. SuperDARN is a collection of radars funded by the national scientific funding
724 agencies of Australia, Canada, China, France, Italy, Japan, Norway, South Africa, United
725 Kingdom, and the United States of America. The Fort Hays SuperDARN radars are maintained
726 and operated by Virginia Tech under support by NSF grant AGS-1935110. The King Salmon and
727 Prince George radars are operated under support of NSF grant AGS--2125323 from the Upper
728 Atmospheric Facilities Program, and by the Canada Foundation for Innovation, Innovation
729 Saskatchewan and the Canadian Space Agency, respectively. We thank the many different groups
730 operating magnetometer arrays for providing data for this study, including the THEMIS UCLA
731 magnetometer network (Ground-based Imager and Magnetometer Network for Auroral Studies).
732 The AUTUMNX magnetometer network is funded through the Canadian Space Agency/Geospace
733 Observatory (GO) Canada program, Athabasca University, Centre for Science/Faculty of Science
734 and Technology. The Magnetometer Array for Cusp and Cleft Studies (MACCS) array is
735 supported by the US National Science Foundation grant ATM-0827903 to Augsburg College. The
736 Solar and Terrestrial Physics (STEP) magnetometer file storage is at the Department of Earth and
737 Planetary Physics, University of Tokyo and maintained by Kanji Hayashi (hayashi@grl.s.u-
738 tokyo.ac.jp). The McMAC Project is sponsored by the Magnetospheric Physics Program of
739 National Science Foundation through grant AGS-0245139. The ground magnetic stations are
740 operated by the Technical University of Denmark, National Space Institute (DTU Space). The

741 IMAGE magnetometer stations are maintained by 10 institutes from Finland, Germany, Norway, Poland, Russia, Sweden, Denmark, and Iceland. The Canadian Space Science Data Portal is funded in part by the Canadian Space Agency contract numbers 9 F007-071429 and 9 F007-070993. The Canadian Magnetic Observatory Network (CANMON) is maintained and operated by the Geological Survey of Canada. David R. Themens's contribution to this work is supported in part through CSA grant no. 21SUSTCHAI and through the United Kingdom Natural Environment Research Council (NERC) EISCAT3D: Fine-scale structuring, scintillation, and electrodynamics (FINESSE) (NE/W003147/1) and DRivers and Impacts of Ionospheric Variability with EISCAT-3D (DRIIVE) (NE/W003368/1) projects. James M. Weygand acknowledges NASA grant: 80NSSC18K0570, 80NSSC18K1220, NASA contract: 80GSFC17C0018 (HPDE), NAS5-02099(THEMIS). Shibaji Chakraborty thanks the National Science Foundation for support under grant AGS-1935110.

Financial support. David R. Themens's contribution to this work is supported in part through CSA grant no. 21SUSTCHAI and through the United Kingdom Natural Environment Research Council (NERC) EISCAT3D: Fine-scale structuring, scintillation, and electrodynamics (FINESSE) (NE/W003147/1) and DRivers and Impacts of Ionospheric Variability with EISCAT-3D (DRIIVE) (NE/W003368/1) projects. J. Chum was funded by T-FORS project by European Commission (number SEP 210818055) and by the Johannes Amos Comenius Programme (P JAC), project No. CZ.02.01.01/00/22_008/0004605, Natural and anthropogenic georisks". James M. Weygand is supported by the NASA grant: 80NSSC18K0570, 80NSSC18K1220, NASA contract: 80GSFC17C0018 (HPDE), NAS5-02099(THEMIS). Shibaji Chakraborty is supported by the National Science Foundation under grant AGS-1935110.

References

Afraimovich, E. L., Kosogorov, E. A., Leonovich, L. A., Pala martchouk, K. S., Perevalova, N. P., and Pirog, O. M.: Determining parameters of large-scale traveling ionospheric disturbances of auroral origin using GPS-arrays, J. Atmos. Sol.-Terr. Phy., 62, 553–565, https://doi.org/10.1016/S1364-6826(00)00011-0, 2000.

Alexander, M. J.: A simulated spectrum of convectively generated gravity waves: Propagation from the tropopause to the mesopause and effects on the middle atmosphere, Journal of Geophysical Research: Atmospheres, 101(D1), pp. 1571–1588. doi: https://doi.org/10.1029/95JD02046, 1996.

Amm, O., Engebretson, M. J., Hughes, T., Newitt, L., Viljanen, A., and Watermann, J.: A traveling convection vortex event study: Instantaneous ionospheric equivalent currents, estimation of field-aligned currents, and the role of induced currents, J. Geophys. Res., 107, 1334, doi:10.1029/2002JA009472, 2002.

779

780 Azeem, I. et al.: Multisensor profiling of a concentric gravity wave event propagating from the
781 troposphere to the ionosphere, Geophysical Research Letters, 42(19), pp. 7874–7880. doi:
782 https://doi.org/10.1002/2015GL065903, 2015.

783 Azeem, I. and Barlage, M.: Atmosphere-ionosphere coupling from convectively generated
784 gravity waves, Advances in Space Research, 61(7), pp. 1931–1941. doi:
785 https://doi.org/10.1016/j.asr.2017.09.029, 2018.

786 Azeem, I.: Asymmetry of near-noncentric traveling ionospheric disturbances due to Doppler-
787 shifted atmospheric gravity waves, Frontiers in Astronomy and Space Sciences, 8,
788 https://doi.org/10.3389/fspas.2021.690480, 2021.

789 Balthazor, R. L. and J., R.: A study of atmospheric gravity waves and travelling iono-spheric
790 disturbances at equatorial latitudes, Ann. Geophys., 15. Available at: http://www.ann-
791 geophys.net/15/1048/1997/, 1997.

792 Becker, E., Goncharenko, L., Harvey, V. L., & Vadas, S. L.: Multi-step vertical coupling during
793 the January 2017 sudden stratospheric warming. Journal of Geophysical Research: Space
794 Physics, 127, e2022JA030866. https://doi.org/10.1029/2022JA030866, 2022.

795
796 Becker, E., Vadas, S. L., Bossert, K., Harvey, V. L., Zülicke, C., & Hoffmann, L.: A High-
797 resolution whole-atmosphere model with resolved gravity waves and specified large-scale
798 dynamics in the troposphere and stratosphere. Journal of Geophysical Research: Atmospheres,
799 127, e2021JD035018. https://doi.org/10.1029/2021JD035018, 2022.

800 Belcher, J. W., and Davis, L., Jr.: Large-amplitude Alfvén waves in the interplanetary medium,
801 2. J. Geophys. Res., 76, 3534–3563, 1971.

802 Bertin, F., Testud, J., Kersley, L., and Rees, P. R.: The meteorological jet stream as a source of
803 medium scale gravity waves in the thermosphere: an experimental study, Journal of Atmospheric
804 and Terrestrial Physics, 40(10), pp. 1161–1183. doi: https://doi.org/10.1016/0021-
805 9169(78)90067-3, 1978.

806 Bertin, F., Testud, J. and Kersley, L.: Medium scale gravity waves in the ionospheric F-region
807 and their possible origin in weather disturbances, Planetary and Space Science, 23(3), pp. 493–
808 507. doi: https://doi.org/10.1016/0032-0633(75)90120-8, 1975.

809

810 Bossert, K., Vadas, S. L., Hoffmann, L., Becker, E., Harvey, V. L., & Bramberger, M.:
811 Observations of stratospheric gravity waves over Europe on 12 January 2016: The role of the polar
812 night jet. Journal of Geophysical Research: Atmospheres, **125**, e2020JD032893.
813 https://doi.org/10.1029/2020JD032893, 2020.
814
815
816 Bossert, K., Paxton, L. J., Matsuo, T., Goncharenko, L., Kumari, K., & Conde, M.: Large-scale
817 traveling atmospheric and ionospheric disturbances observed in GUVI with multi-instrument

818 validations. Geophysical Research Letters, 49, e2022GL099901.
819 https://doi.org/10.1029/2022GL099901, 2022.
820

821 Bristow, W. A., Greenwald, R. A. and Samson, J. C.: Identification of high-latitude acoustic
822 gravity wave sources using the Goose Bay HF Radar, Journal of Geophysical Research: Space
823 Physics, 99(A1), pp. 319–331. doi: https://doi.org/10.1029/93JA01470, 1994.

824 Cai, H. T., Yin, F., Ma, S. Y., and McCrea, I. W.: Observations of AGW/TID propagation across
825 the polar cap: a case study, Annales Geophysicae, 29(8), pp. 1355–1363. doi: 10.5194/angeo-29-
826 1355-2011, 2011.

827 Cheng, P-H., Lin, C., Otsuka, Y., Liu, H., Rajesh, P. K.,Chen, C-H., Lin, J-T., and Chang, M. T.:
828 Statistical study of medium-scale traveling ionospheric disturbances in low-latitude ionosphere
829 using an automatic algorithm, Earth Planets Space 73, 105, https://doi.org/10.1186/s40623-021-
830 01432-1, 2021.

831 Cherniak, I. and Zakharenkova, I.: Large-scale traveling iono spheric disturbances origin and
832 propagation: Case study of the December 2015 geomagnetic storm, Space Weather, 16, 1377–
833 1395, https://doi.org/10.1029/2018SW001869, 2018.

834 Chimonas, G.: The equatorial electrojet as a source of long period travelling ionospheric
835 disturbances, Planetary and Space Science, 18(4), pp. 583–589. doi:
836 https://doi.org/10.1016/0032-0633(70)90133-9, 1970.

837 Chimonas, G. and Hines, C. O.: Atmospheric gravity waves launched by auroral currents,
838 Planetary and Space Science, 18(4), pp. 565–582. doi: 10.1016/0032-0633(70)90132-7, \1970.

839 Chum J., Podolská K.: 3D analysis of GW propagation in the ionosphere. Geophysical Research
840 Letters, 45, 11,562–11,571, https://doi.org/10.1029/2018GL079695, 2018.
841

842 Chum, J., Podolská, K., Rusz, J., Baše, J., and Tedoradze, N.: Statistical investigation of gravity
843 wave characteristics in the ionosphere, Earth, Planets and Space, 73(1), p. 60. doi:
844 10.1186/s40623-021-01379-3, 2021.

845 Crowley, G. and Williams, P. J. S.: Observations of the source and propagation of atmospheric
846 gravity waves, Nature, 328(6127), pp. 231–233. doi: 10.1038/328231a0, 1988.

847 Deng, Y., Heelis, R., Lyons, L. R., Nishimura, Y., and Gabrielse, C.: Impact of flow bursts in the
848 auroral zone on the ionosphere and thermosphere, Journal of Geophysical Research: Space
849 Physics, 124, 10459–10467. https://doi.org/10.1029/2019JA026755, 2020.

850 Dungey, J. W.: Interplanetary Magnetic Field and the Auroral Zones. Phys. Rev. Lett. 6, 47–48.
851 https://doi.org/10.1103/PhysRevLett.6.47, 1961.

852 Dungey, J. W.: Origin of the concept of reconnection and its application to the magnetopause: A
853 historical view, Physics of the Magnetopause. Geophysical Monograph 90, edited by P. Song,
854 B.U.O. Sonnerup, and M.F. Thomsen, pp. 17–19, AGU, Washington, D.C., 1995.

855   Frissell, N. A., Baker, J. B. H., Ruohoniemi, J. M., Gerrard, A. J., Miller, E. S., Marini, J. P.,
856   West, M. L., and Bristow, W. A.: Climatology of medium-scale traveling ionospheric
857   disturbances observed by the midlatitude Blackstone SuperDARN radar, Journal of Geophysical
858   Research: Space Physics, 119(9), pp. 7679–7697. doi: https://doi.org/10.1002/2014JA019870,
859   2014.

860   Frissell, N. A., Baker, J. B. H., Ruohoniemi, J. M., Greenwald, R. A., Gerrard, A. J., Miller, E.
861   S., and West, M. L.: Sources and characteristics of medium-scale traveling ionospheric
862   disturbances observed by high-frequency radars in the North American sector, Journal of
863   Geophysical Research: Space Physics, 121(4), pp. 3722–3739,
864   https://doi.org/10.1002/2015JA022168, 2016.

865   Goncharenko, L., Harvey, V. L., Cullens, C., Becker, E., Zhang, S.-R., and Coster, A.: Influence
866   of stratospheric gravity waves on TID activity at middle latitudes, in EGU General Assembly
867   Conference Abstracts, pp. EGU22-6823, doi: 10.5194/egusphere-egu22-6823, 2022.

868   Gonzalez, W. D., Joselyn, J. A., Kamide, Y., Kroehl, H. W., Rostoker, G., Tsurutani, B. T., and
869   Vasyliunas, V. M.: What is a geomagnetic storm?, Journal of Geophysical Research: Space
870   Physics, 99(A4), pp. 5771–5792, doi: https://doi.org/10.1029/93JA02867, 1994.

871   Hajkowicz, L. A.: Auroral electrojet effect on the global occurrence pattern of large scale
872   travelling ionospheric disturbances, Planetary and Space Science, 39(8), pp. 1189–1196., doi:
873   https://doi.org/10.1016/0032-0633(91)90170-F, 1991.

874   Heinselman, C. J. and Nicolls, M. J.: A Bayesian approach to electric field and E-region neutral
875   wind estimation with the Poker Flat Advanced Modular Incoherent Scatter Radar, Radio Science,
876   43(5). doi: https://doi.org/10.1029/2007RS003805, 2008.

877   Hersbach, H., Bell, B., Berrisford, P., Hirahara, S., Horányi, A., Muñoz-Sabater, J., Nicolas, J.,
878   Peubey, C., Radu, R., Schepers, D., Simmons, A., Soci, C., Abdalla, S., Abellan, X., Balsamo,
879   G., Bechtold, P., Biavati, G., Bidlot, J., Bonavita, M., De Chiara, G., Dahlgren, P., Dee, D.,
880   Diamantakis, M., Dragani, R., Flemming, J., Forbes, R., Fuentes, M., Geer, A., Haimberger, L.,
881   Healy, S., Hogan, R. J., Hólm, E., Janisková, M., Keeley, S., Laloyaux, P., Lopez, P., Lupu, C.,
882   Radnoti, G., de Rosnay, P., Rozum, I., Vamborg, F., Villaume, S., and Thépaut, J.-N.: The ERA5
883   global reanalysis, Q. J. R. Met. Soc., 146(730), pp. 1999–2049. doi:
884   https://doi.org/10.1002/qj.3803, 2020.

885   Hines, C. O.: Internal Atmospheric Gravity Waves At Ionospheric Heights, Canadian Journal of
886   Physics, 38(11), pp. 1441–1481. doi: 10.1139/p60-150, 1960.

887   Hocke, K. and Schlegel, K.: A review of atmospheric gravity waves and travelling ionospheric
888   disturbances: 1982-1995, Annales Geophysicae, 14(9), pp. 917–940, doi: 10.1007/s00585-996-
889   0917-6, 1996.

890   Huang, C.-S., Sofko, G. J., Kustov, A. V, MacDougall, J. W., Andre, D. A., Hughes, W. J., and
891   Papitashvili, V. O.: Quasi-periodic ionospheric disturbances with a 40-min period during
892   prolonged northward interplanetary magnetic field, Geophysical Research Letters, 27(12), pp.
893   1795–1798, doi: https://doi.org/10.1029/1999GL003731, 2000.

894   Huang, C.-S., Andre, D. A. and Sofko, G. J.: Observations of solar wind directly driven auroral
895   electrojets and gravity waves, Journal of Geophysical Research: Space Physics, 103(A10), pp.
896   23347–23356. doi: https://doi.org/10.1029/98JA02297, 1998.

897   Hunsucker, R. D.: Atmospheric gravity waves generated in the high-latitude ionosphere: A
898   review, Reviews of Geophysics, 20(2), pp. 293–315, doi: 10.1029/RG020i002p00293, 1982.

899

900   Inchin, P. A., Bhatt, A., Bramberger, M., Chakraborty, S., Debchoudhury, S., and Heale, C.:
901   Atmospheric and ionospheric responses to orographic gravity waves prior to the December 2022
902   cold air outbreak. Journal of Geophysical Research: Space Physics, 129, e2024JA032485.
903   https://doi.org/10.1029/2024JA032485, 2024.

904   van de Kamp, M., Pokhotelov, D. and Kauristie, K.: TID characterised using joint effort of
905   incoherent scatter radar and GPS, Annales Geophysicae, 32(12), pp. 1511–1532, doi:
906   10.5194/angeo-32-1511-2014, 2014.

907   King, J. H. and Papitashvili, N.: Solar wind spatial scales in and comparisons of hourly Wind
908   and ACE plasma and magnetic field data, Journal of Geophysical Research, 110(A2), p. A02104.
909   doi: 10.1029/2004JA010649, 2005.

910   Koch, S. E. and Dorian, P. B.: A Mesoscale Gravity Wave Event Observed during CCOPE. Part
911   III: Wave Environment and Probable Source Mechanisms, Monthly Weather Review, 116(12),
912   pp. 2570–2592. doi: https://doi.org/10.1175/1520-0493(1988)116<2570:AMGWEO>2.0.CO;2,
913   1988.

914   Koch, S. E. and OHandley, C.: Operational Forecasting and Detection of Mesoscale Gravity
915   Waves, Weather and Forecasting, 12(2), pp. 253–281, doi: https://doi.org/10.1175/1520-
916   0434(1997)012<0253:OFADOM>2.0.CO;2, 1997.

917   Lewis, R. V, Williams, P. J. S., Millward, G. H., and Quegan, S.: The generation and
918   propagation of atmospheric gravity waves from activity in the auroral electrojet, Journal of
919   Atmospheric and Terrestrial Physics, 58(6), pp. 807–820, doi: https://doi.org/10.1016/0021-
920   9169(95)00075-5, 1996.

921   Mayr, H. G., Harris, I., Varosi, F., and Herrero, F. A.: Global Excitation of Wave Phenomena in
922   a Dissipative Multiconstituent Medium. 1. Transfer Function of the EarthS Thermosphere,
923   Journal of Geophysical Research, 89(A12), pp. 10929–10959, doi: 10.1029/JA089iA12p10929,
924   1984a.

925   Mayr, H. G., Harris, I., Varosi, F., and Herrero, F. A.: Global Excitation of Wave Phenomena in
926   a Dissipative Multiconstituent Medium - 2. Impulsive Perturbations in the EarthS Thermosphere,
927   Journal of Geophysical Research, 89(A12), pp. 10961–10986. doi: 10.1029/JA089iA12p10961,
928   1984b.

929   Mayr, H. G., Talaat, E. R. and Wolven, B. C.: Global propagation of gravity waves generated
930   with the whole atmosphere transfer function model, Journal of Atmospheric and Solar-Terrestrial
931   Physics, 104, pp. 7–17, doi: 10.1016/j.jastp.2013.08.001, 2013.

McWilliams, K. A., Yeoman, T. K. and Provan, G.: A statistical survey of dayside pulsed ionospheric flows as seen by the CUTLASS Finland HF radar, Annales Geophysicae, 18(4), pp. 445–453, doi: 10.1007/s00585-000-0445-8, 2000.

Milan, S. E., Gosling, J. S., and Hubert, B.: Relationship between interplanetary parameters and the magnetopause reconnection rate quantified from observations of the expanding polar cap, J. Geophys. Res., 117, A03226, doi:10.1029/2011JA017082 2012.

Millward, G.: A resonance effect in AGWs created by periodic recurrent bursts in the auroral electric field, Annales Geophysicae, 12(1), pp. 94–94, 1994.

Millward, G. H., Quegan, S., Moffett, R. J., Fuller-Rowell, T. J., and Rees, D.: A modelling study of the coupled ionospheric and thermospheric response to an enhanced high-latitude electric field event, Planetary and Space Science, 41(1), pp. 45–56, doi: 10.1016/0032-0633(93)90016-U, 1993a.

Millward, G. H., Moffett, R. J., Quegan, S., and Fuller-Rowell, T. J.: Effects of an atmospheric gravity wave on the midlatitude ionospheric F layer, Journal of Geophysical Research: Space Physics, 98(A11), pp. 19173–19179. doi: 10.1029/93ja02093, 1993b.

Mrak, S., Semeter, J., Nishimura, Y., Hirsch, M., and Sivadas, N.: Coincidental TID Production by Tropospheric Weather During the August 2017 Total Solar Eclipse, Geophysical Research Letters, 45(20), pp. 10,903-910,911, doi: https://doi.org/10.1029/2018GL080239, 2018.

Munteanu, C., Hamada, A., and Mursula, K.: High-speed solar wind streams in 2007-2008: Turning on the Russell-McPherron effect, Journal of Geophysical Research: Space Physics, 124, https://doi. org/10.1029/2019JA026846, 2019.

Negrea, C., Munteanu, C., and Echim, M. M.: Global ionospheric response to a periodic sequence of HSS/CIR events during the 2007–2008 solar minimum, Journal of Geophysical Research: Space Physics, 126, e2020JA029071, https://doi.org/10.1029/2020JA029071, 2021.

Nicolls, M. J., and Heinselman , C. J.: Three-dimensional measurements of traveling ionospheric disturbances with the Poker Flat Incoherent Scatter Radar, Geophys. Res. Lett., 34, L21104, doi:10.1029/2007GL031506, 2007.

Nishimura, Y., Zhang, S. R., Lyons, L. R., Deng, Y., Coster, A. J., Moen, J. I., Clausen, L. B., Bristow, W. A. and Nishitani, N.: Source region and propagation of dayside large-scale traveling ionospheric disturbances, Geophysical Research Letters, 47, e2020GL089451. https://doi.org/10.1029/2020GL089451, 2020.

Nishioka, M., Tsugawa, T., Kubota, M., and Ishii, M: Concentric waves and short-period oscillations observed in the ionosphere after the 2013 Moore EF5 tornado, Geophysical Research Letters, 40(21), pp. 5581–5586, doi: https://doi.org/10.1002/2013GL057963, 2013.

Nishitani, N., Ruohoniemi, J. M., Lester, M., Baker, J. B. H., Koustov, A. V., Shepherd, S. G., Chisham, G., Hori, T., Thomas, E. G., Makarevich, R. A., Marchaudon, A., Ponomarenko, P., Wild, J. A., Milan, S. E., Bristow, W. A., Devlin, J., Miller, E., Greenwald, R. A., Ogawa, T., and Kikuchi, T.: Review of the accomplishments of mid-latitude Super Dual Auroral Radar

970   Network (SuperDARN) HF radars, Progress in Earth and Planetary Science, 6(1), p. 27, doi:
971   10.1186/s40645-019-0270-5, 2019.

972   Nykiel, G., Ferreira, A., Günzkofer, F., Iochem, P., Tasnim, S., and Sato, H.: Large-Scale
973   Traveling Ionospheric Disturbances over the European sector during the geomagnetic storm on
974   March 23–24, 2023: Energy deposition in the source regions and the propagation characteristics.
975   Journal of Geophysical Research: Space Physics, 129, e2023JA032145,
976   https://doi.org/10.1029/2023JA032145, 2024.
977

978   Plougonven, R. and Teitelbaum, H.: Comparison of a large-scale inertia-gravity wave as seen in
979   the ECMWF analyses and from radiosondes, Geophysical Research Letters, 30(18), doi:
980   https://doi.org/10.1029/2003GL017716, 2003.

981   Plougonven, R. and Zhang, F.: Internal gravity waves from atmospheric jets and fronts, *Reviews*
982   *of Geophysics,* 52(1), pp. 33–76. doi: https://doi.org/10.1002/2012RG000419, 2014.

983   Press, W. H. and Teukolsky, S. A.: Savitzky-Golay Smoothing Filters, Comput. Phys. 4 (6):
984   669–672. https://doi.org/10.1063/1.4822961, 1990.

985   Prikryl, P., MacDougall, J. W., Grant, I. F., Steele, D. P., Sofko, G. J., and Greenwald, R. A.:
986   Polar patches generated by solar wind Alfvén wave coupling to the dayside magnetosphere,
987   Advances in Space Research, 23(10). doi: 10.1016/S0273-1177(99)00390-7, 1999.

988   Prikryl, P., Provan, G., McWilliams, K. A., and Yeoman, T. K.: Ionospheric cusp flows pulsed
989   by solar wind Alfvén waves, Annales Geophysicae, 20(2), doi: 10.5194/angeo-20-161-2002,
990   2002.

991   Prikryl, P., Muldrew, D. B., Sofko, G. J., and Ruohoniemi, J. M.: Solar wind Alfvén waves: A
992   source of pulsed ionospheric convection and atmospheric gravity waves, Annales Geophysicae,
993   23(2), pp. 401–417, doi: 10.5194/angeo-23-401-2005, 2005.

994   Prikryl, P., Gillies, R. G., Themens, D. R., Weygand, J. M., Thomas, E. G., and Chakraborty, S.:
995   Multi-instrument observations of polar cap patches and traveling ionospheric disturbances
996   generated by solar wind Alfvén waves coupling to the dayside magnetosphere, Annales
997   Geophysicae, 40(6), pp. 619–639, doi: 10.5194/angeo-40-619-2022, 2022.

998   Rae, I. J., Fenrich, F. R.,Lester, M., McWilliams, K. A., and Scudder, J. D.: Solar wind
999   modulation of cusp particle signatures and their associated ionospheric flows, *J. Geophys. Res.*,
1000   109, A03223, doi:10.1029/2003JA010188, 2004.

1001   Richmond, A. D.: Gravity wave generation, propagation, and dissipation in the thermosphere,
1002   Journal of Geophysical Research, 83(A9), p. 4131, doi: 10.1029/ja083ia09p04131, 1978.

1003   Richmond, A.D.: Large-amplitude gravity wave energy production and dissipation in the
1004   thermosphere, Journal of Geophysical Research: Space Physics, 84(A5), 1880–1890.
1005   https://doi.org/10.1029/JA084iA05p01880, 1979.

1006   Samson, J. C., Greenwald, R. A., Ruohoniemi, J. M., and Baker, K. B.: High-frequency radar
1007   observations of atmospheric gravity waves in the high latitude ionosphere, Geophysical Research
1008   Letters 16, 875–878, 1989.

1009   Samson, J. C, Greenwald, R. A., Ruohoniemi, J. M., Frey, A., Baker, K. B.: Goose bay radar
1010   observations of earth-reflected, atmospheric gravity-waves in the high-latitude ionosphere, J.
1011   Geophys. Res. 95(A6):7693–7709, https://doi.org/10.1029/JA095iA06p07693, 1990.

1012   Smith, C. W., LHeureux, J., Ness, N. F., Acuña, M. H., Burlaga, L. F., and Scheifele, J.: The
1013   ACE Magnetic Fields Experiment, *Space Science Reviews*, 86(1), pp. 613–632. doi:
1014   10.1023/A:1005092216668, 1998.

1015   SuperDARN Data Analysis Working Group, Thomas, E. G., Reimer, A. S., Bland, E. C., Burrell,
1016   A. G., Grocott, A., Ponomarenko, P. V., Schmidt, M. T., Shepherd, S. G., Sterne, K. T., and
1017   Walach, M.-T.: SuperDARN Radar Software Toolkit (RST) 5.0 (v5.0). Zenodo.
1018   https://doi.org/10.5281/zenodo.7467337, 2022.

1019   Testud, J.: Gravity waves generated during magnetic substorms, Journal of Atmospheric and
1020   Terrestrial Physics, 32(11), pp. 1793–1805, doi: 10.1016/0021-9169(70)90137-6, 1970.

1021   Themens, D. R., Jayachandran, P. T., Langley, R. B., MacDougall, J. W., and Nicolls, M. J.:
1022   Determining receiver biases in GPS-derived total electron content in the auroral oval and polar
1023   cap region using ionosonde measurements, GPS Solutions, 17(3), pp. 357–369. doi:
1024   10.1007/s10291-012-0284-6, 2013.

1025   Themens, D. R., Watson, C., Žagar, N., Vasylkevych, S., Elvidge, S., McCaffrey, A., Prikryl, P.,
1026   Reid, B., Wood, A., and Jayachandran, P. T.: Global Propagation of Ionospheric Disturbances
1027   Associated With the 2022 Tonga Volcanic Eruption, Geophysical Research Letters, 49(7), p.
1028   e2022GL098158, doi: https://doi.org/10.1029/2022GL098158, 2022.

1029   Themens, D. R., Jayachandran, P. T. and Langley, R. B.: The nature of GPS differential receiver
1030   bias variability: An examination in the polar cap region, Journal of Geophysical Research: Space
1031   Physics, 120(9), pp. 8155–8175, doi: https://doi.org/10.1002/2015JA021639, 2015.

1032   Tsurutani, B. T., and Gonzalez, W. D.: 1987 The cause of high-intensity long-duration
1033   continuous AE activity (HILDCAAs): Interplanetary Alfvén wave trains, Planet. Space
1034   Sci., 35(4), 405–412, doi:10.1016/0032-0633(87)90097-3, 1987

1035   Tsurutani, B. T., Gould, T., Goldstein, B. E., Gonzalez, W. D., and Sugiura, M.: Interplanetary
1036   Alfvén waves and auroral (substorm) activity: Imp 8, J. Geophys. Res.*,* 95(A3), 2241–2252,
1037   doi:10.1029/ja095ia03p02241, 1990.

1038   Tsurutani, B. T., Gonzalez, W. D., Gonzalez, A. L. C., Tang, F., Arballo, J. K., and Okada, M.:
1039   Interplanetary origin of geomagnetic activity in the declining phase of the solar cycle, *J.*
1040   *Geophys. Res. Space Phys.,* 100(A11), 21717–21733, doi:10.1029/95ja01476, 1995.

1041   Tsurutani, B. T., et al.: Corotating solar wind streams and recurrent geomagnetic activity: A
1042   review, J. Geophys. Res., 111, A07S01, doi:10.1029/2005JA011273, 2006.Uccellini, L. W. and
1043   Koch, S. E.: The Synoptic Setting and Possible Energy Sources for Mesoscale Wave

1044   Disturbances, Monthly Weather Review, 115(3), pp. 721–729, doi: https://doi.org/10.1175/1520-
1045   0493(1987)115<0721:TSSAPE>2.0.CO;2, 1987.

1046   Vadas, S. L. and Nicolls, M. J.: Using PFISR measurements and gravity wave dissipative
1047   theory to determine the neutral thermospheric winds, Geophys. Res. Lett., 35, L02105,
1048   doi:10.1029/2007GL031522, 2008.

1049   Vadas, S. L. and Azeem, I.: Concentric secondary gravity waves in the thermosphere and
1050   ionosphere over the continental United States on March 25–26, 2015 from deep Convection.
1051   Journal of Geophysical Research: Space Physics, 126, e2020JA028275, https://
1052   doi.org/10.1029/2020JA028275

1053   Vadas, S. L., Becker, E., Bossert, K., Baumgarten, G., Hoffmann, L., and Harvey, V. L.: Secondary
1054   gravity waves from the stratospheric polar vortex over ALOMAR observatory on 12–14 January
1055   2016: Observations and modeling. Journal of Geophysical Research: Atmospheres, 128,
1056   e2022JD036985.   https://doi.org/10.1029/2022JD036985,
1057   2023.https://doi.org/10.1029/2022JD036985, 2023.
1058

1059   Waldock, J. A. and Jones, T. B. (1987) Source regions of medium scale travelling ionospheric
1060   disturbances observed at mid-latitudes, Journal of Atmospheric and Terrestrial Physics, 49(2),
1061   pp. 105–114. doi: https://doi.org/10.1016/0021-9169(87)90044-4, 2021.

1062   Weygand, J. M., Amm, O., Viljanen, A., Angelopoulos, V., Murr, D., Engebretson, M. J.,
1063   Gleisner, H., and Mann, I.: Application and validation of the spherical elementary currents
1064   systems technique for deriving ionospheric equiv alent currents with the North American and
1065   Greenland ground magnetometer arrays, J. Geophys. Res., 116, A03305,
1066   https://doi.org/10.1029/2010JA016177, 2011.
1067

1068   Weygand, J.M., Amm, O., Angelopoulos, V., Milan, S.E., Grocott, A., Gleisner, H., Stolle, C.:
1069   Comparison Between SuperDARN Flow Vectors and Equivalent Ionospheric Currents from
1070   Ground Magnetometer Arrays, J. Geophys. Res., 117, A05325, doi:10.1029/2011JA017407,
1071   2012.
1072

1073   Weygand, J. M., and Wing, S.: Comparison of DMSP and SECS region-1 and region-2
1074   ionospheric current boundary, J. Atmos. Solar Terr. Phys., 143, 8-13, 2016.
1075

1076   Williams, P. J. S., Virdi, T. S., Lewis, R. V., Lester, M., Rodger, A. S., McCrea, I. W., and
1077   Freeman, K. S. C.: Worldwide atmospheric gravity-wave study in the European sector 1985–
1078   1990, Journal of Atmospheric and Terrestrial Physics, 55(4–5), pp. 683–696, doi: 10.1016/0021-
1079   9169(93)90014-P, 1993.

1080   Yang, Y.-H., Chao, J.-K. and Lee, L.-C.: On the Walén Relation for Alfvénic Fluctuations in
1081   Interplanetary Space, The Astrophysical Journal, 904(2), p. 195, doi: 10.3847/1538-4357/abbf55,
1082   2020.

1083   Yu, Y., Wang, W. and Hickey, M. P.: Ionospheric signatures of gravity waves produced by the
1084   2004 Sumatra and 2011 Tohoku tsunamis: A modeling study, Journal of Geophysical Research:
1085   Space Physics, 122(1), pp. 1146–1162, doi: https://doi.org/10.1002/2016JA023116, 2017.

1086 Zhang, S.-R., Erickson, P. J., Goncharenko, L. P., Coster, A. J., Rideout, W., and Vierinen, J.:
1087 Ionospheric Bow Waves and Perturbations Induced by the 21 August 2017 Solar Eclipse,
1088 Geophysical Research Letters, 44(24), pp. 12,12-67,73, doi:
1089 https://doi.org/10.1002/2017GL076054, 2017.

1090 Zhang, S.-R., Coster, A. J., Erickson, P. J., Goncharenko, L. P., Rideout, W., & Vierinen, J.:
1091 Traveling ionospheric disturbances and ionospheric perturbations associated with solar flares in
1092 September 2017. Journal of Geophysical Research: Space Physics, 124, 5894–5917,
1093 https://doi.org/10.1029/2019JA026585, 2019.

1094

1095

1096   **Figures**
1097
1098

1099
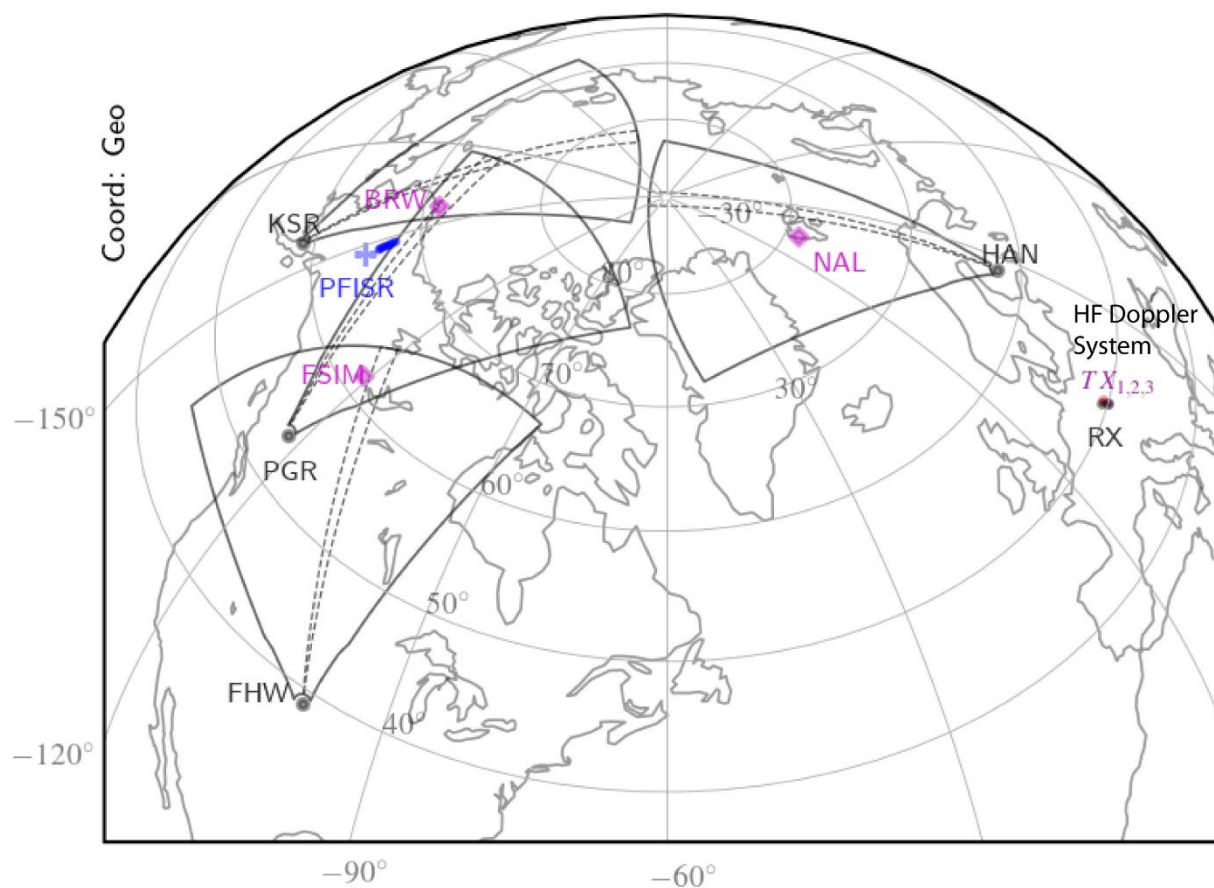
1100   **Figure 1:** The field-of-views of SuperDARN radars in King Salmon (KSR), Prince George
1101   (PGR) Fort Hayes West (FHW) and Hankasalmi (HAN). The Poker Flats Incoherent Scatter
1102   Radar (PFISR) beam 2 range gates footprints are shown in blue color. Also, the ground
1103   magnetometers in Barrow (BRW), Fort Simpson (FSIM) and Ny Ålesund (NAL) and locations
1104   of transmitters and a receiver of the HF Doppler sounding system operating in the Czech
1105   Republic are shown.
1106
1107
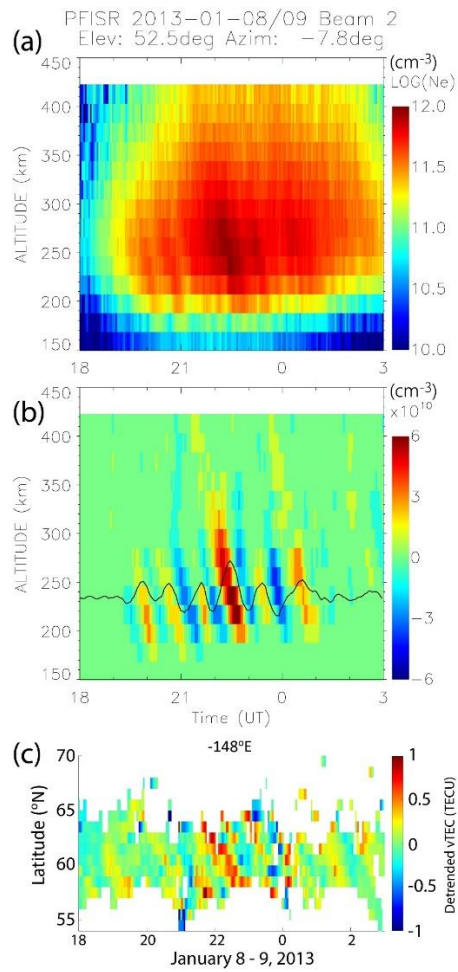
1108
1109 **Figure 2: (a)** Ionospheric density observed by the PFISR radar beam 2 and **(b)** detrended using a
1110 33-point wide Savitzky-Golay filter. **(c)** The detrended GNSS vTEC mapped at latitude bins
1111 along the longitude of PFISR.
1112
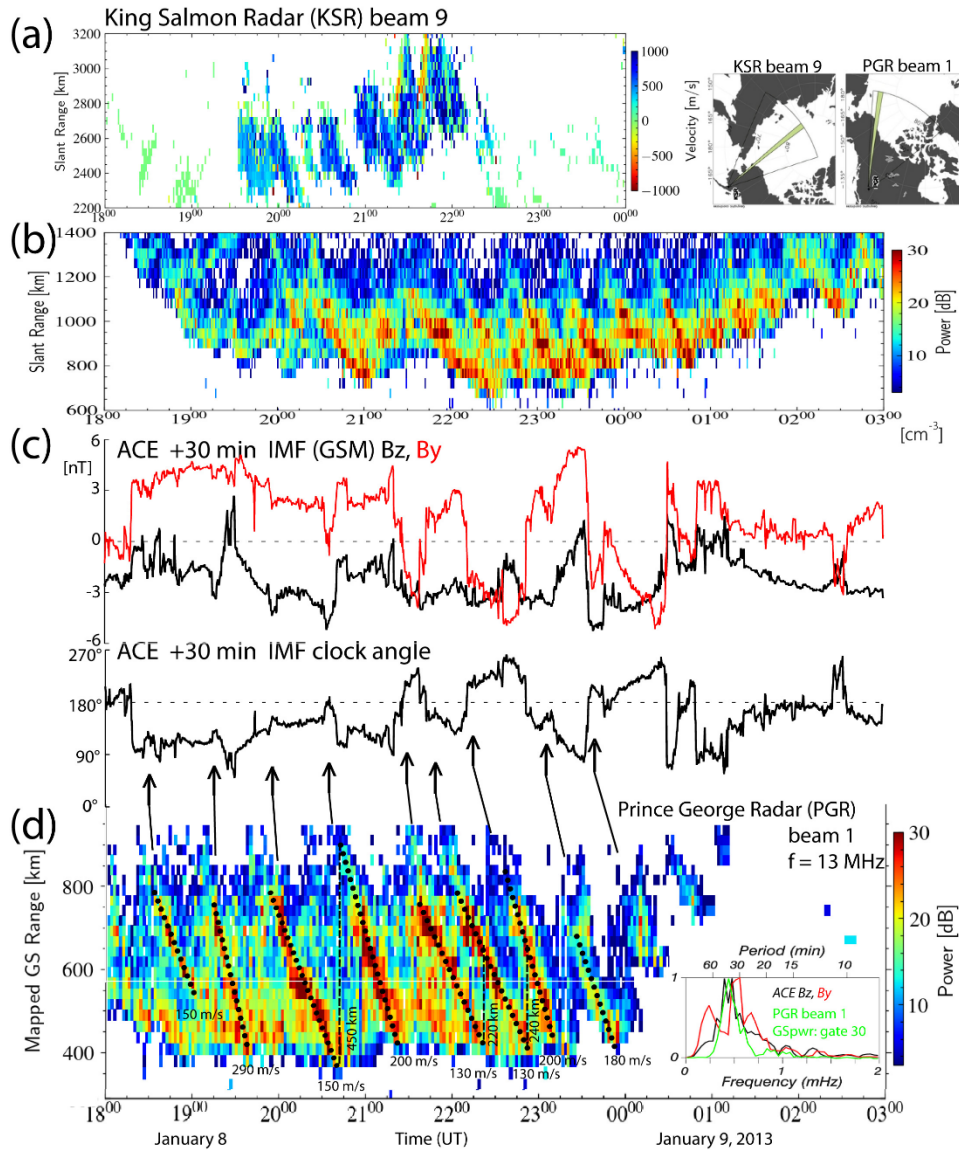
Figure 3: (a) The line-of-sight velocities and **(b)** the sea scatter power as a function of the slant range observed by the KSR radar beam 9. **(c)** The time-shifted time series of the IMF B_z, B_y, and the IMF clock angle observed by ACE spacecraft. **(d)** The mapped ground scatter power observed by the PGR radar beam 1. The arrows indicate southward turning of the IMF. Normalized FFT spectra of the detrended IMF B_z, B_y, and the Prince George radar ground scatter power (beam 1, gate 30, mapped GS range 730 km) are shown in the inset. The estimated TIDs wavelengths and phase velocities are shown.
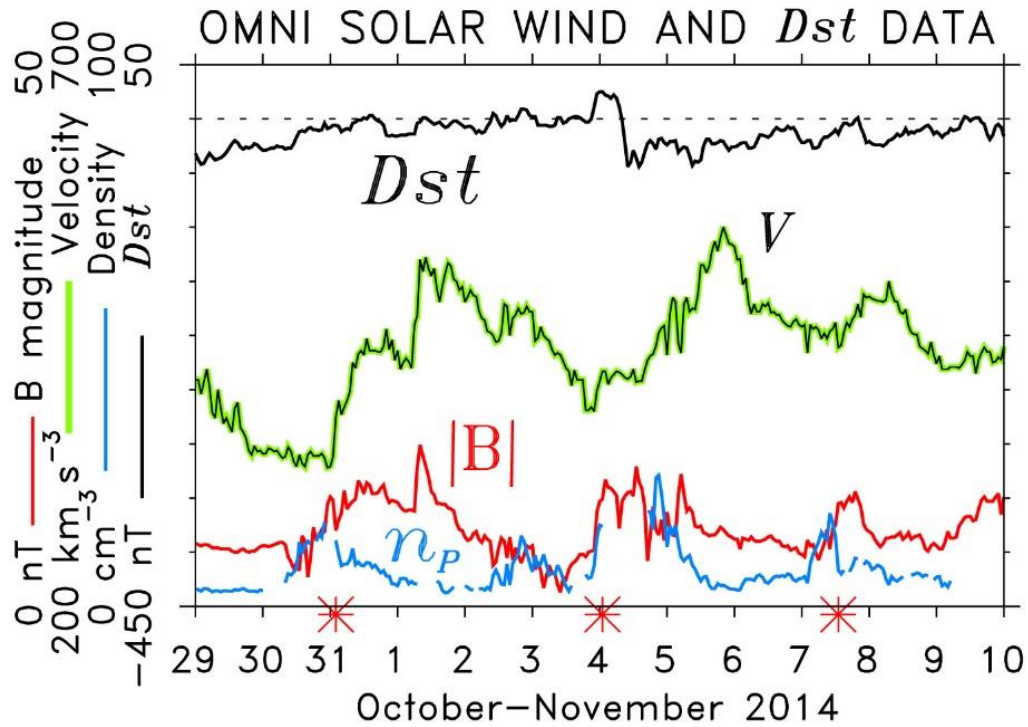
1124
1125 **Figure 4:** The OMNI solar wind velocity *V*, magnetic field magnitude |B|, and proton density n_p
1126 showing three HSS/CIRs on October 31, November 4 and 7 are marked by red asterisks at the
1127 time axis. The ring current *Dst* index is also shown.
1128
1129
1130
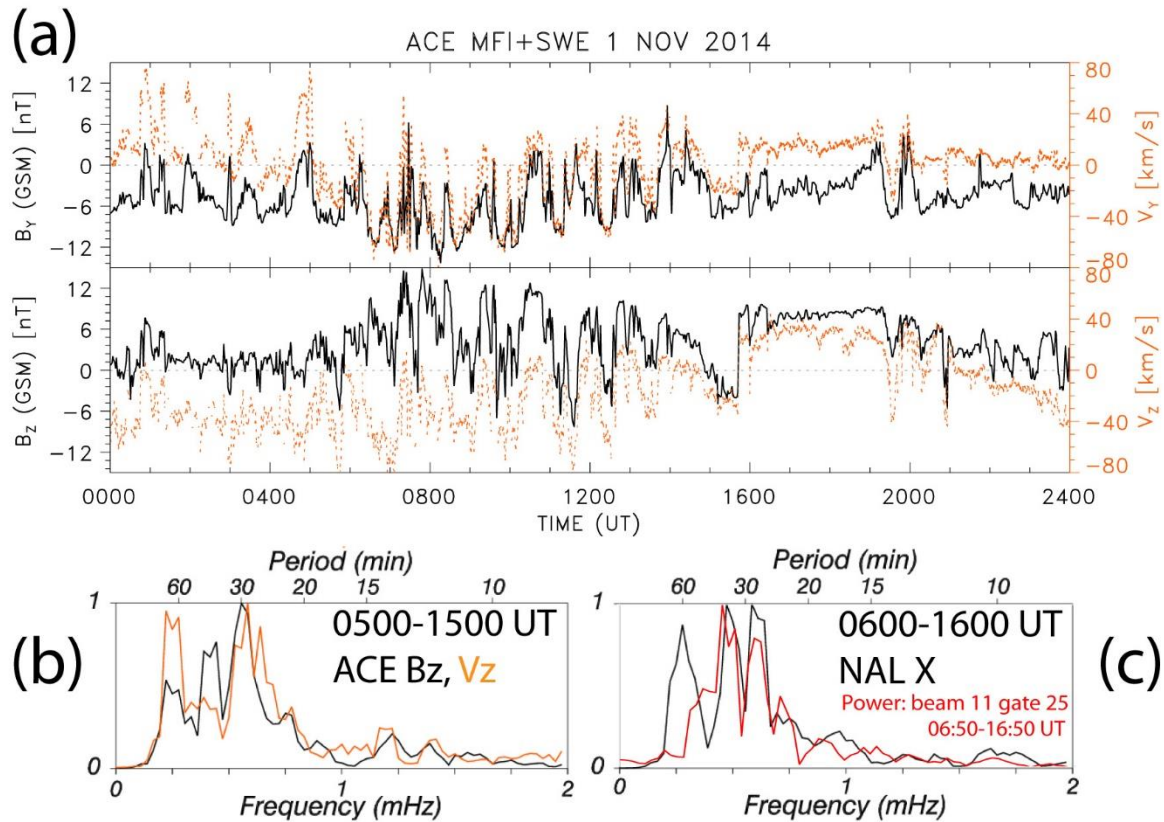
1131
1132
1133 **Figure 5: (a)** The components of the magnetic field and solar wind velocity observed by ACE,
1134 **(b)** the FFT spectra of the detrended time series of IMF B_z and solar velocity V_z, and **(c)** the FFT
1135 spectra of the time series of the X-component of ground magnetic field perturbations in Ny
1136 Ålesund (NAL) and the Hankasalmi radar ground scatter power (beam 11, gate 25, slant range
1137 1305 km).
1138

Rad: han / Beam: 11 / Date: 01 Nov, 2014
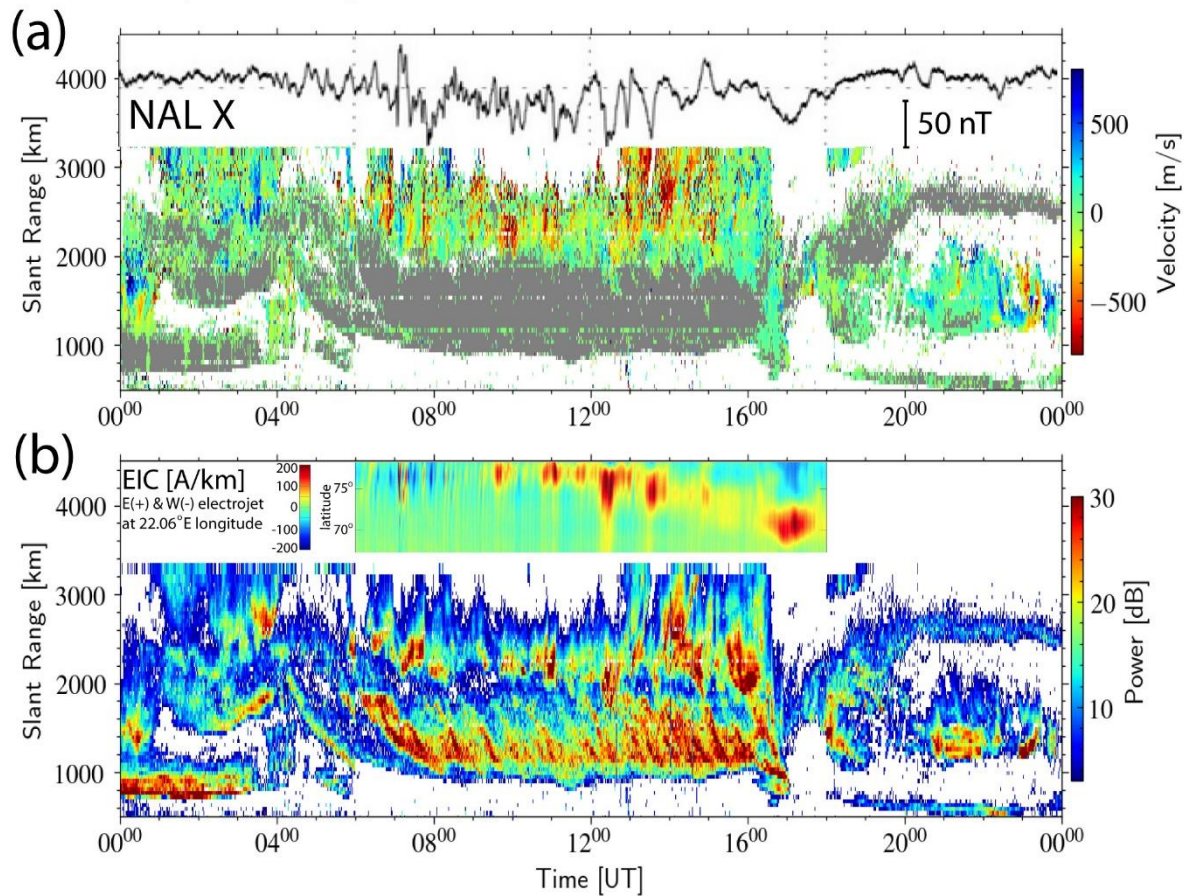
1139
1140 **Figure 6: (a)** The line-of-sight (LoS) velocity and **(b)** the radar scatter power (ground scatter
1141 power shown in grey color in the velocity plot) observed by the Hankasalmi radar beam 11 on
1142 November 1, 2014. The X-component of the ground magnetic field perturbations in Ny Ålesund
1143 (NAL) is superposed representing the fluctuations of ionospheric currents modulated by solar
1144 wind Alfvén waves. 1D equivalent currents estimates that use all IMAGE magnetometers are
1145 also superposed.
1146
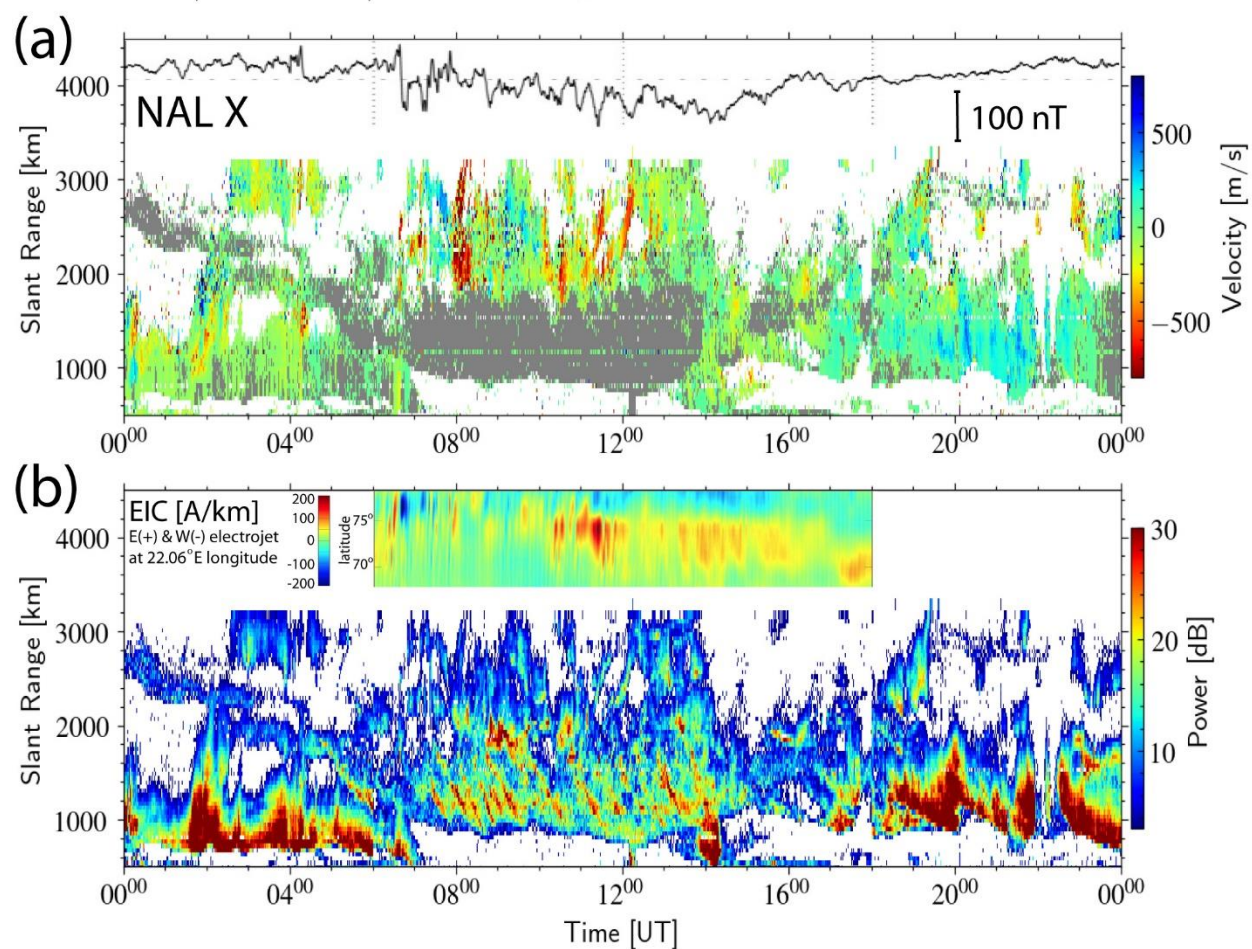
1148   **Figure 7:** The same as Fig. 6 but for November 5, 2014.
1149
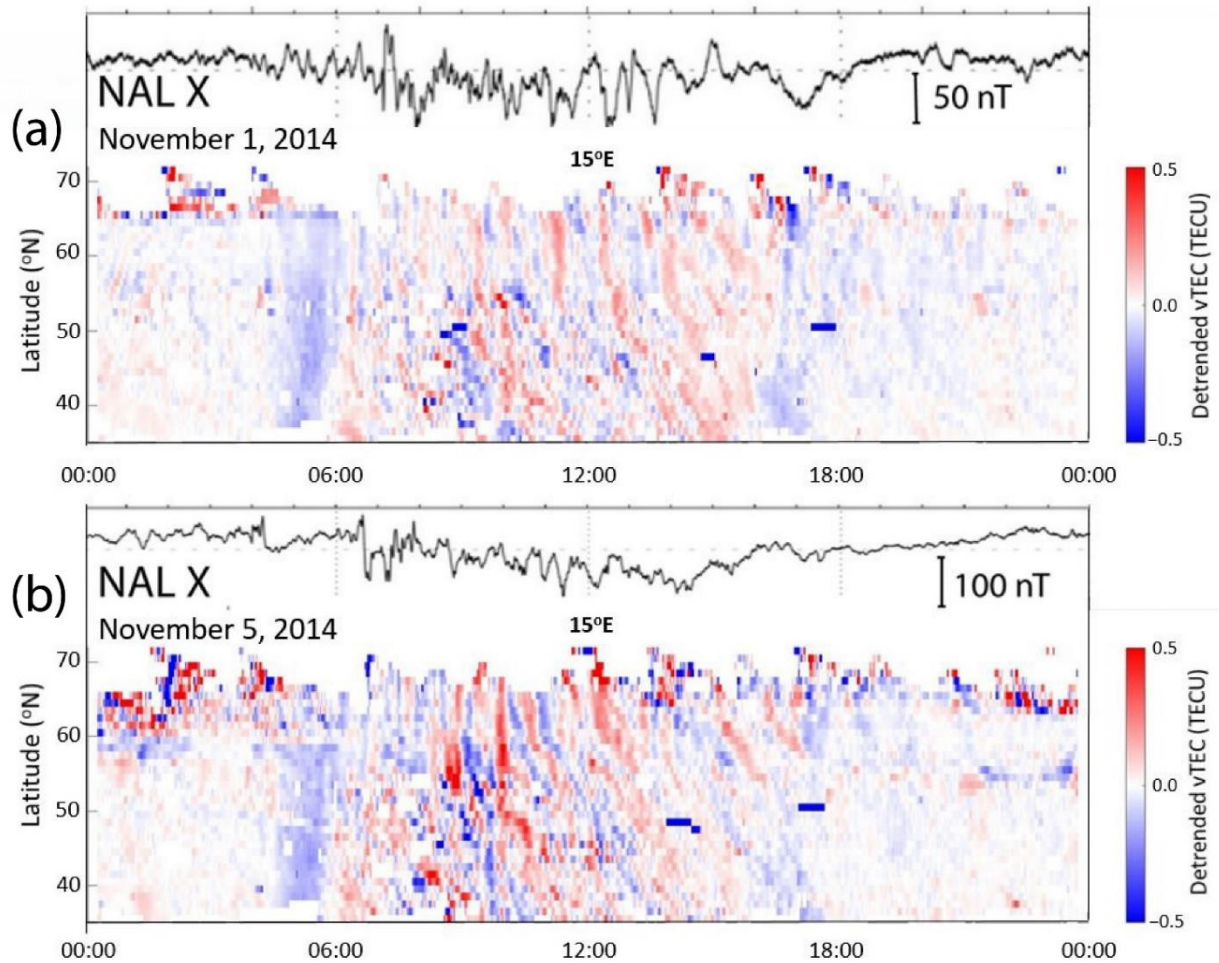
1150
1151 **Figure 8:** The detrended vTEC mapped along longitude of 15°E on **(a)** November 1 and **(b)**
1152 November 5, 2014. The X-component of the ground magnetic field perturbations in Ny Ålesund
1153 (NAL) is superposed.
1154
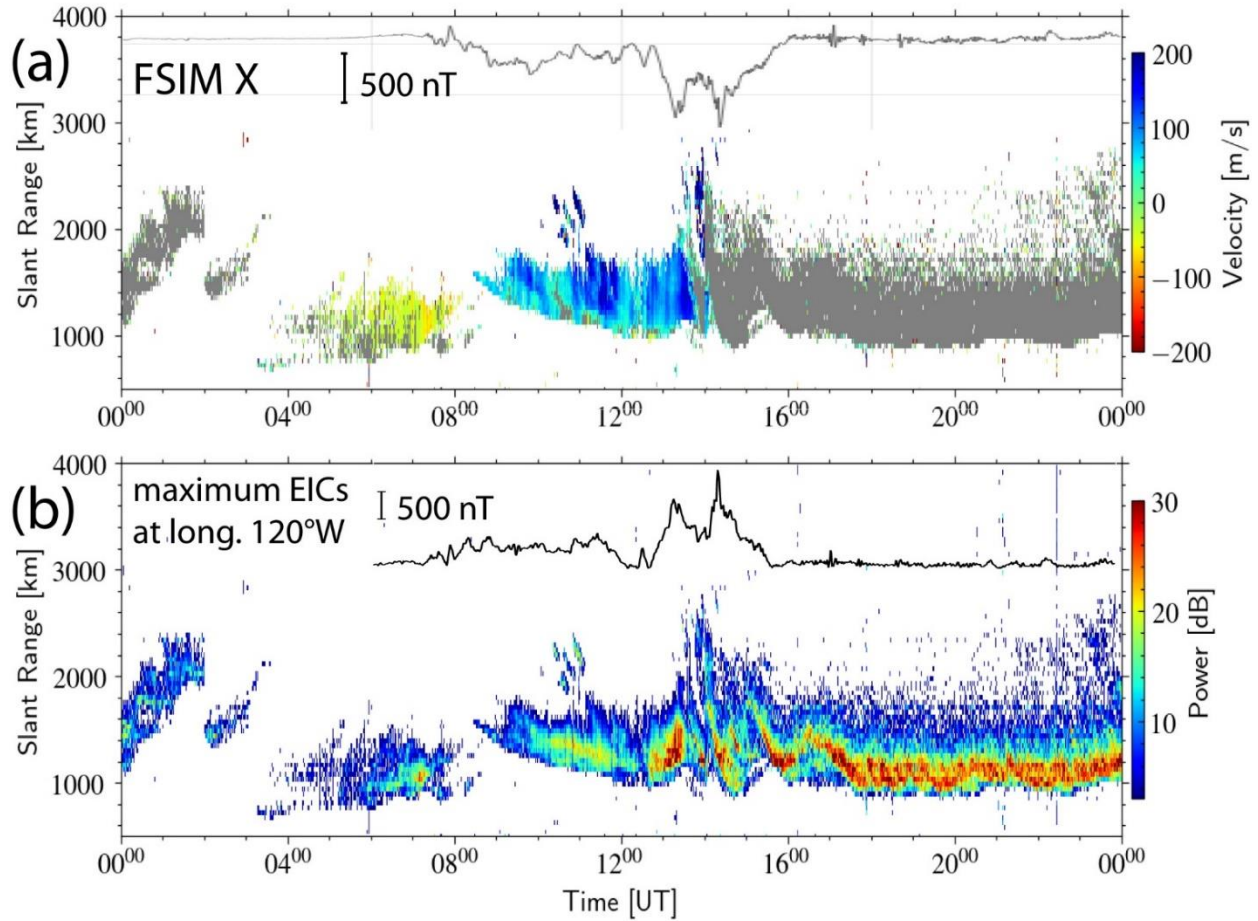
1155
1156 **Figure 9: (a)** The line-of-sight (LoS) velocity and **(b)** the radar scatter power (ground scatter
1157 power shown in grey color in the velocity plot) observed by the Fort Hays West radar beam 12
1158 on November 4, 2014. The X-component of the ground magnetic field perturbations in Fort
1159 Simpson (FSIM) and the maximum EICs at longitude 120°W are superposed.
1160
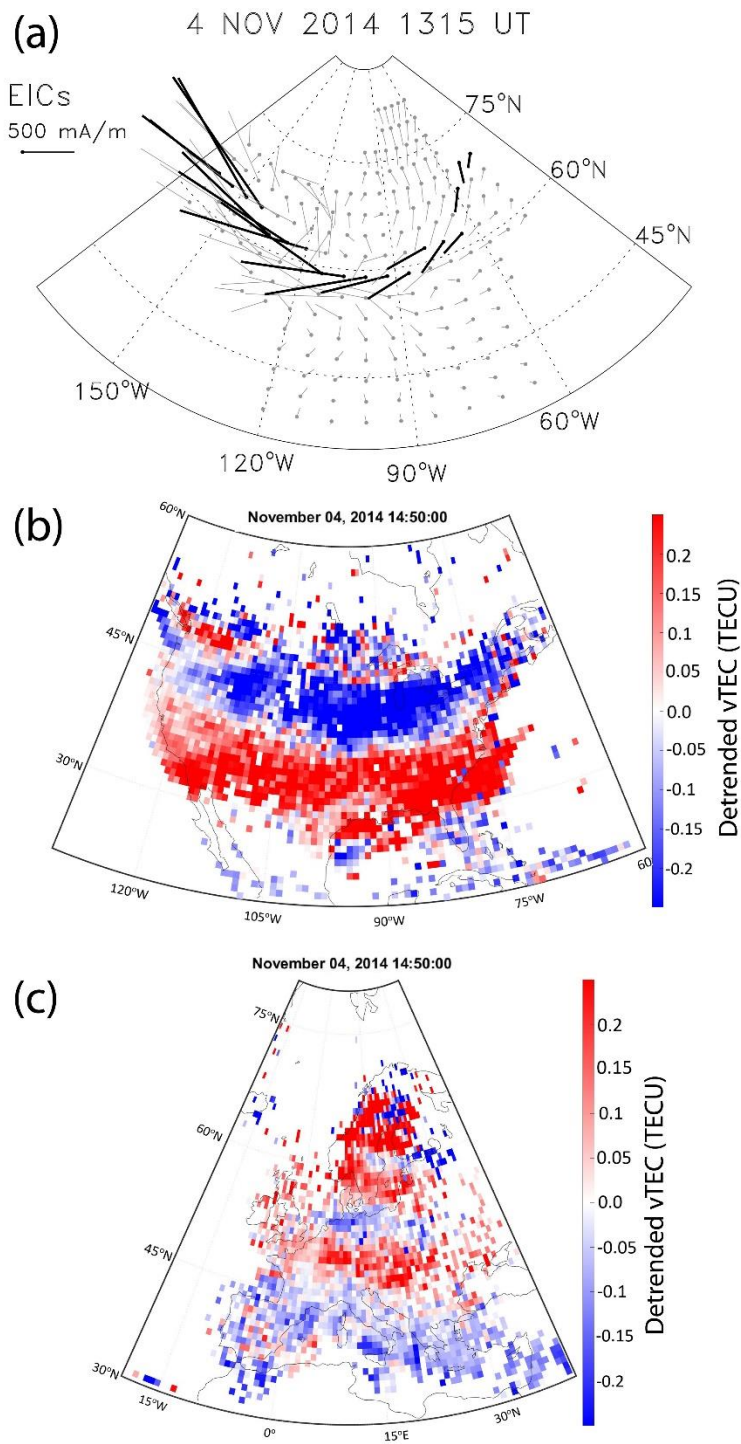
1161
1162   **Figure 10: (a)** The intensification of the westward electrojet over North America, and LSTIDs in
1163   the detrended vTEC maps over **(b)** North America and **(c)** Europe.
1164
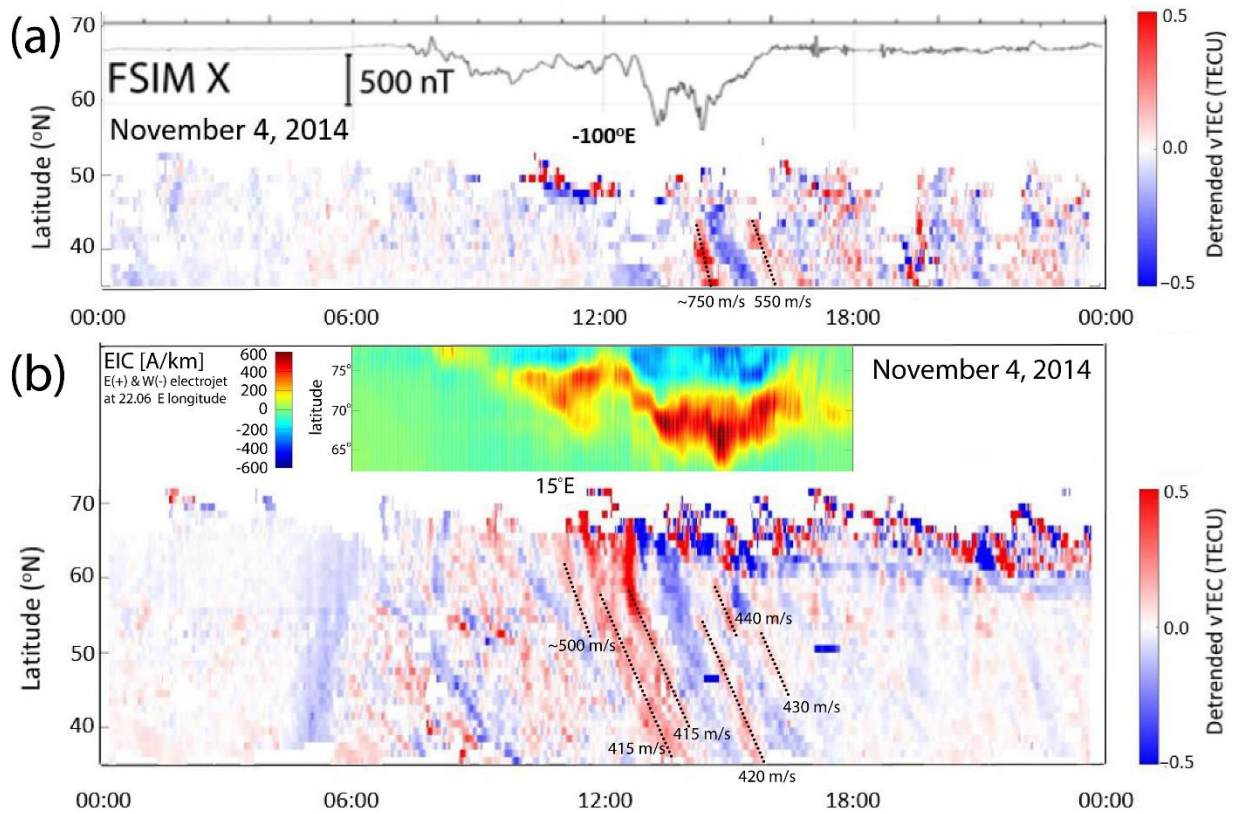
1165
1166 **Figure 11:** The detrended vTEC mapped along longitude of **(a)** 100°W and **(b)** 15°E on
1167 November 4, 2014. The X-component of the ground magnetic field in Fort Simpson (FSIM) and
1168 1D equivalent currents estimates over Scandinavia are superposed.

1169
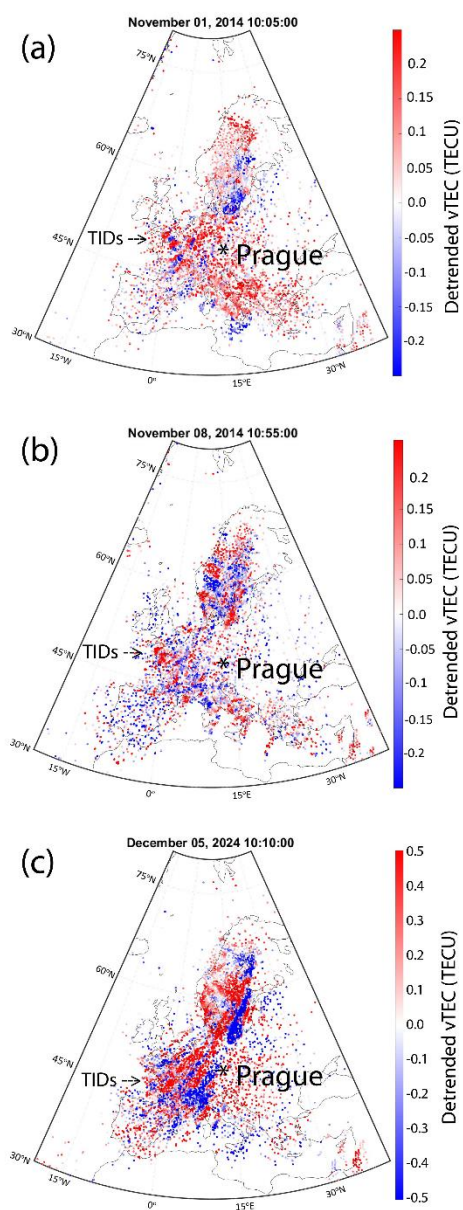
1170
1171
1172   **Figure 12:** The detrended vTEC maps on **(a)** November 1, **(b)** November 8, 2014, and **(c)**
1173   December 5, 2024.
1174
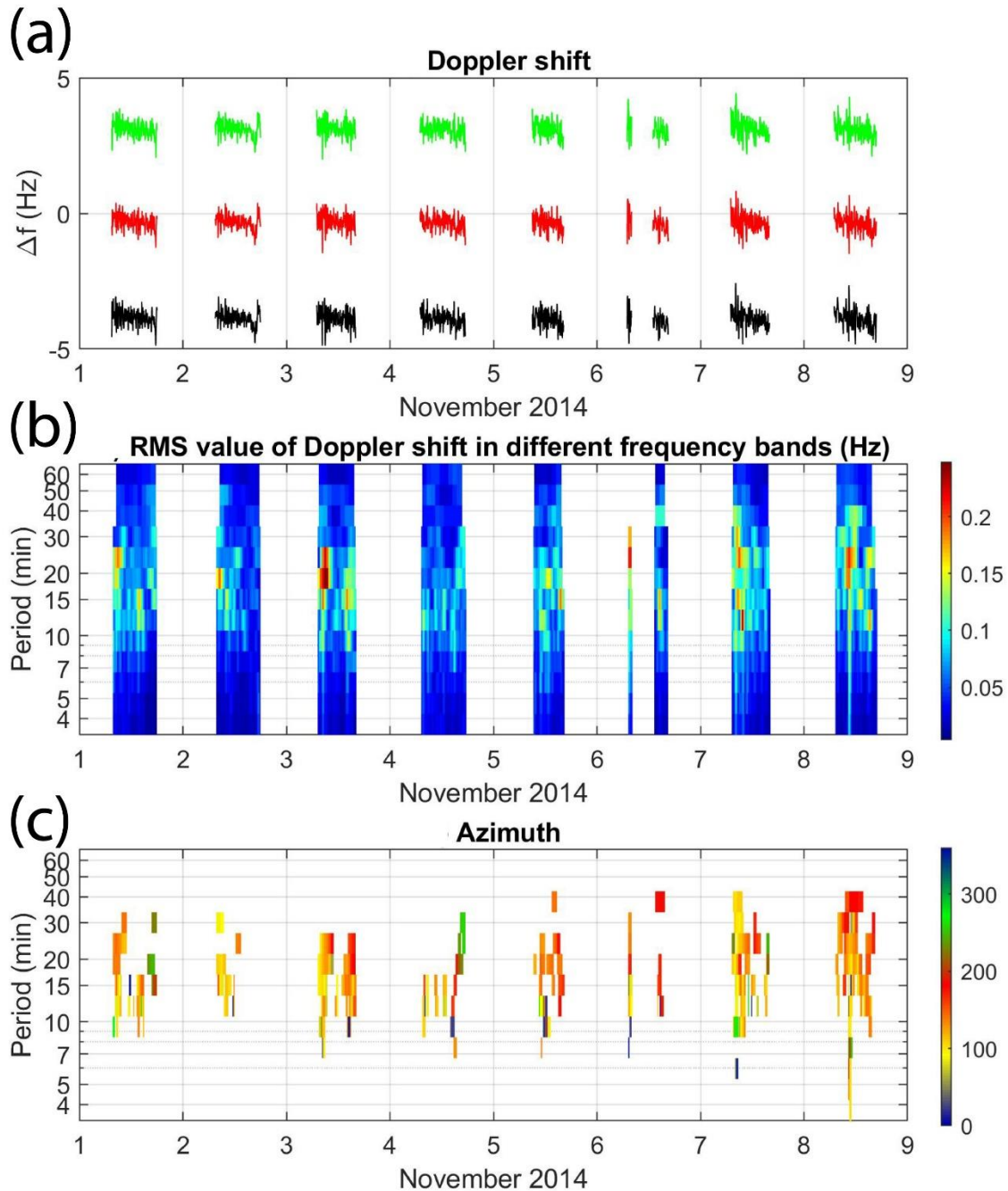
1175
1176 **Figure 13: (a)** Doppler shift frequencies of spectral density maxima for individual transmitter-
1177 receiver pairs (including artificial offsets) from X to Y. **(b)** Dynamic spectra (periodograms) of
1178 Doppler shift signals and **(c)** the propagation azimuth of waves, displayed as function of period
1179 and time for November 1-8, 2014.
1180
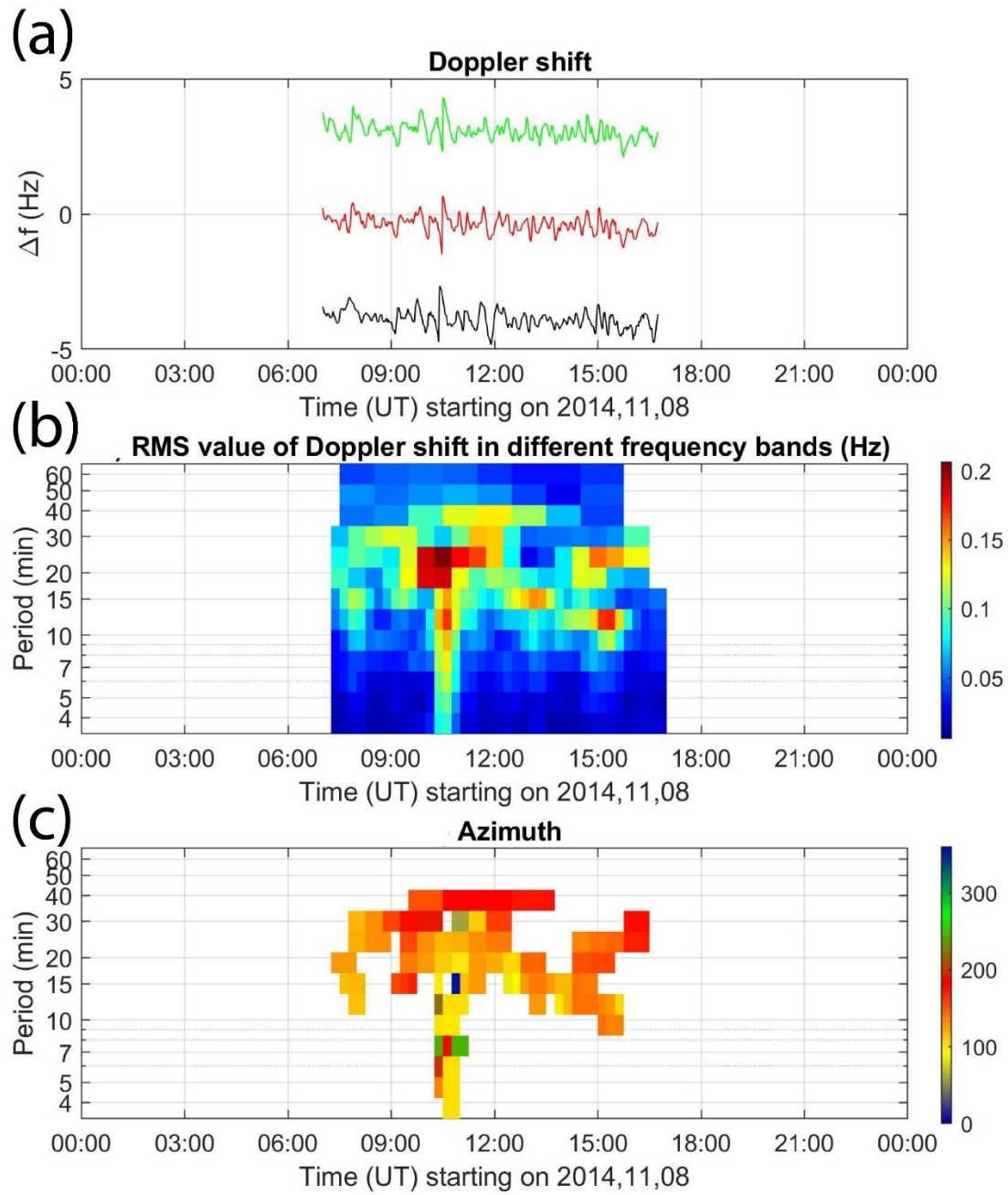
1181
1182   **Figure 14:** The same as Fig. 12 but expanded for November 8, 2014.
1183
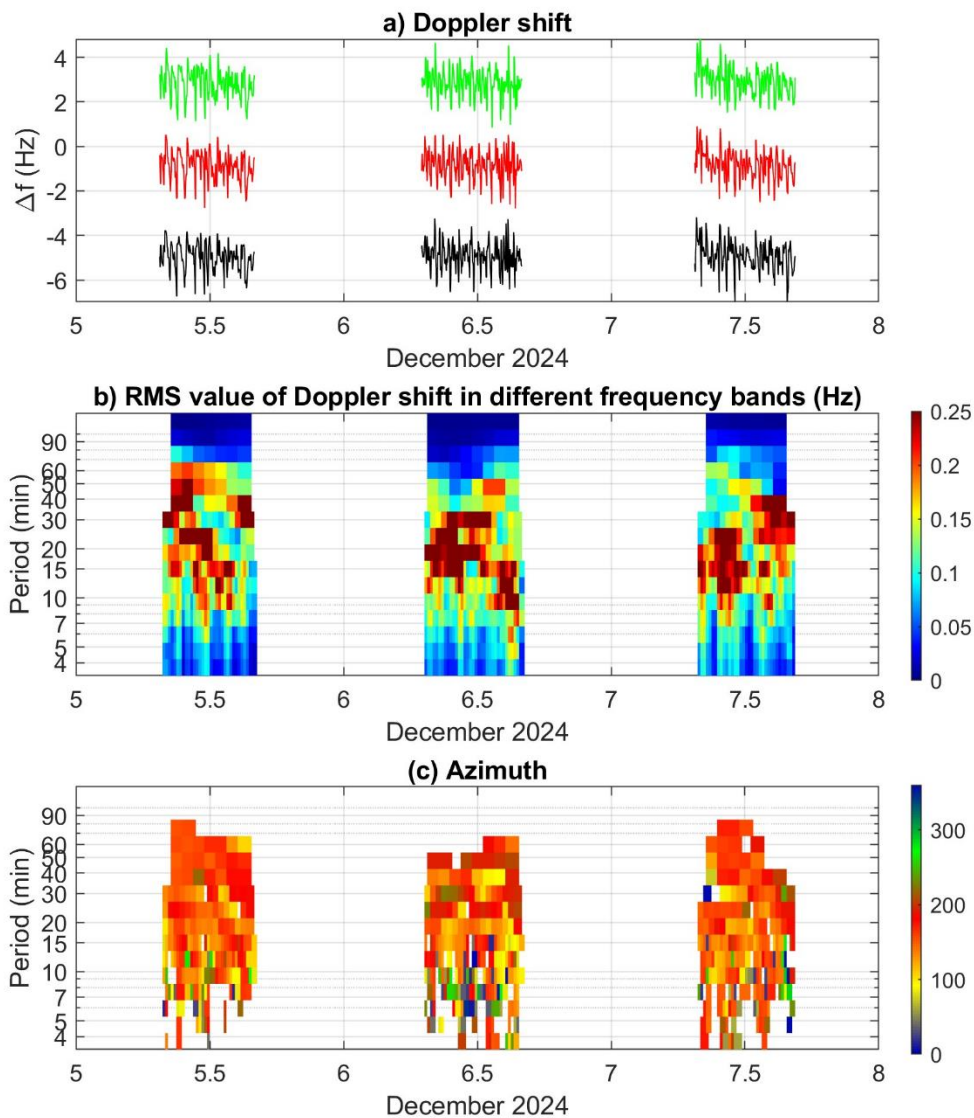
Figure 15: **(a)** Doppler shift frequencies of spectral density maxima for individual transmitter-receiver pairs (including artificial offsets) from X to Y. **(b)** Dynamic spectra (periodograms) of Doppler shift signals and **(c)** the propagation azimuth of waves, displayed as function of period and time for December 5-7, 2024.
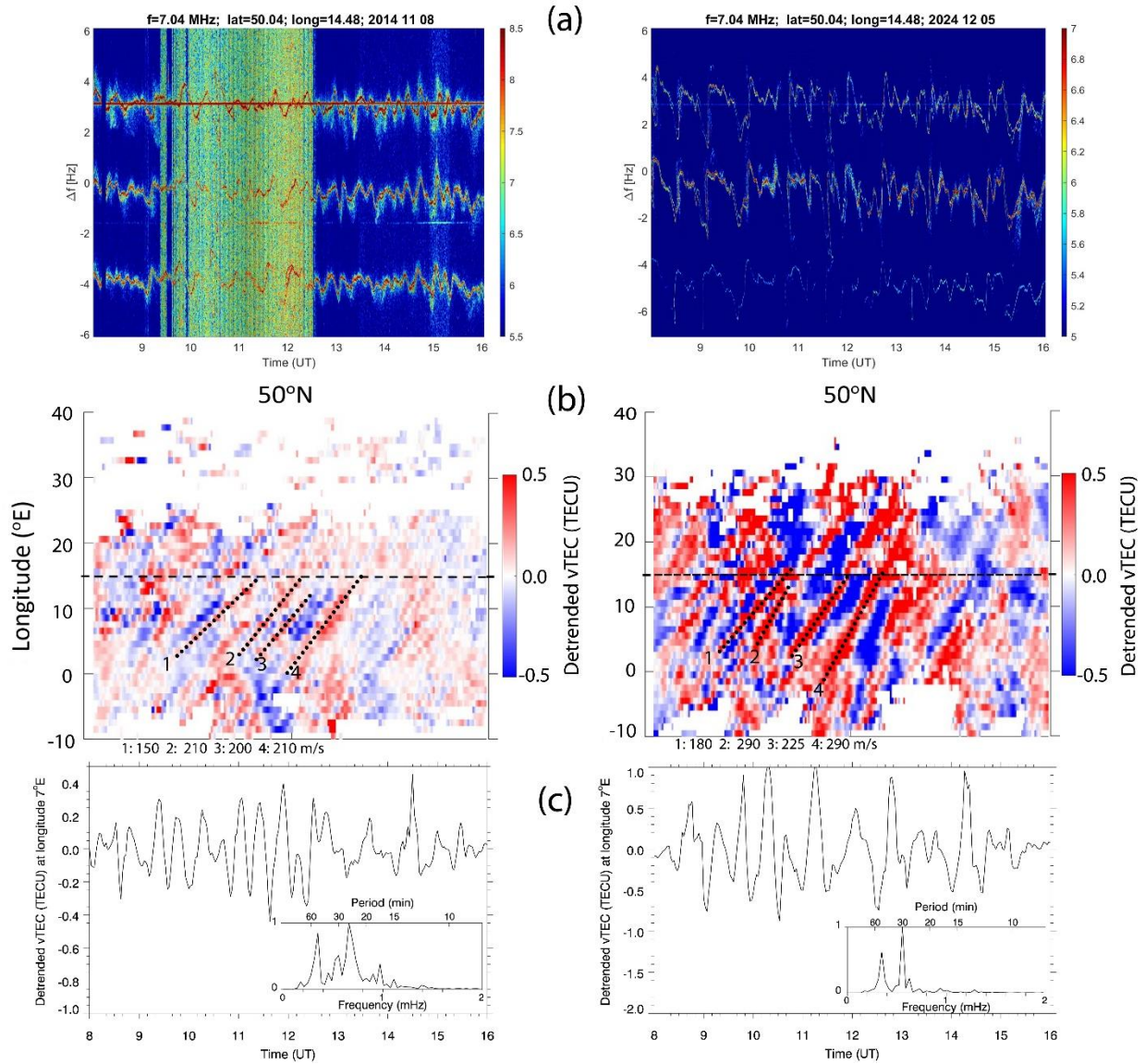
1193
1194 **Figure 16: (a)** The Doppler shift spectrogram recorded at frequency 7.04 MHz on November 8,
1195 2014, and December 5, 2024. **(b)** The detrended vTEC mapped along latitude of 50°N. The
1196 dashed line shows the longitude of Prague. The approximate eastward velocities of TIDs shown
1197 in dotted lines are estimated. **(c)** The detrended vTEC time series at longitude of 7°E and the
1198 normalized FFT spectra.
1199
1200
1201
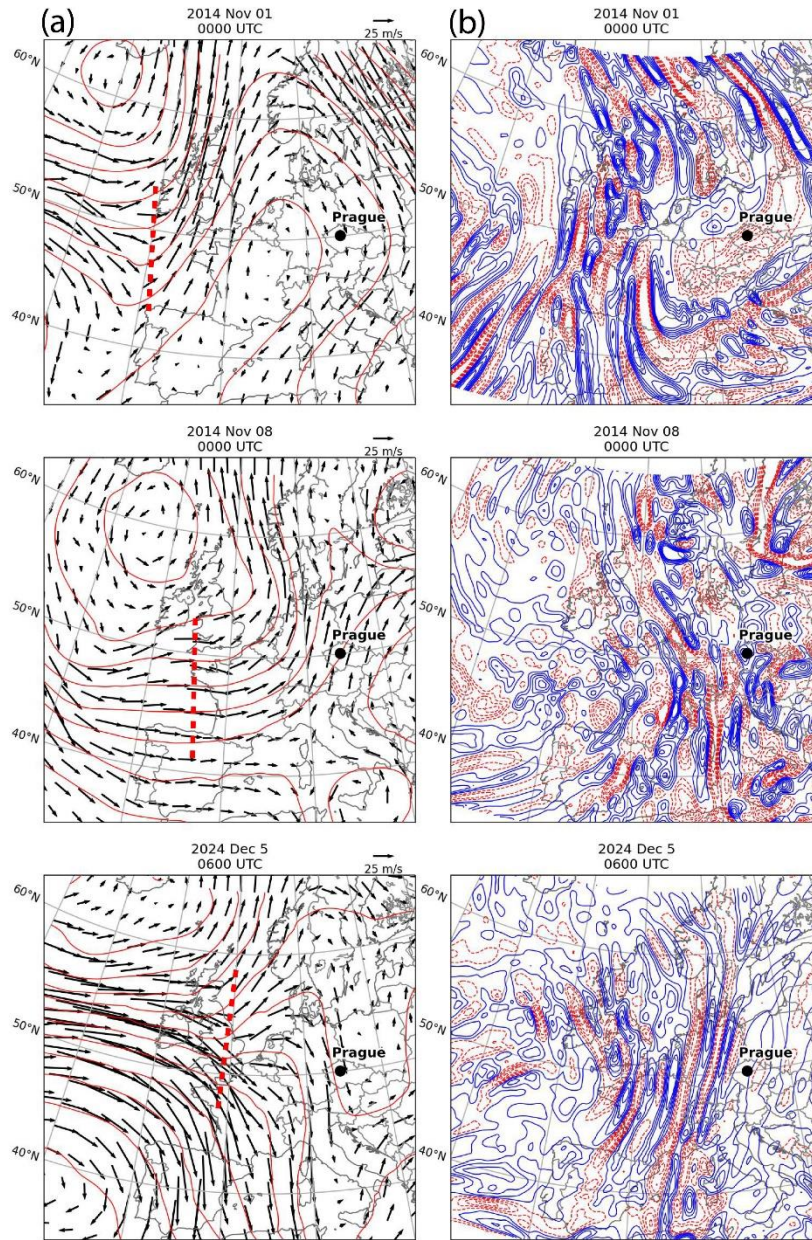
Figure 17: (a) The ERA5 geopotential height (red contours at intervals of 100 m), horizontal winds (m/s) at 300-hPa level, with a probable source region of gravity waves indicated by red dashed line. **(b)** The ERA5 divergence (positive in solid blue line) of the horizontal wind at 150-hPa level, on November 1, November 8, 2014, and December 5, 2024..